Title
Analysis of a flapping foil system for energy harvesting at low Reynolds number

Author
Cho, Hunkee

Publication Date
2011

Peer reviewed|Thesis/dissertation

UNIVERSITY OF CALIFORNIA, SAN DIEGO

Analysis of a Flapping Foil System for Energy Harvesting at low Reynolds number

A Thesis submitted in partial satisfaction of the requirements
for the degree Master of Science

in

Engineering Sciences (Mechanical Engineering)

by

Hunkee Cho

Committee in Charge:

Professor Alison L. Marsden, Chair
Professor Qiang Zhu
Professor Eric Lauga

2011

The Thesis of Hunkee Cho is approved and it is acceptable in quality and form for publication on microfilm and electronically:

Chair

University of California, San Diego

2011

TABLE OF CONTENTS

Signature Page……....iii

Table of Contents …….....iv

List of Abbreviations ……vi

List of Figures …….....vii

List of Tables ……xi

Acknowledgement ……xii

Abstract ……xiii

Chapter 1 Introduction ……1

1.1 Motivation and Goals ……...……1

1.2 Previous Work ……...……3

1.3 Approach and Objectives ……...……...6

1.4 Overview ……...…….…….……..7

Chapter 2 Fundamentals of flapping foil systems……9

2.1 The kinematics of a flapping foil ……..9

2.2 Energy extraction regime ……12

2.3 Extracted power and the power harvesting efficiency……14

Chapter 3 Numerical Method ……...…….17

3.1 Governing equations ……...……....17

3.2 The theory of deforming and sliding meshes ……..19

3.2.1 Conservation equations …….……...19

3.2.2 Dynamic mesh theory …….……..21

3.2.3 Sliding mesh theory …….……24

3.3 Code validation ……..……..25

3.3.1 Dynamic & re-meshing mesh…….….....25

3.3.2 Sliding mesh…….…….28

3.3.3 Flow solver and algorithm……....32

Chapter 4 Energy harvesting performance in uniform flow ……..…….33

4.1 Energy harvesting efficiency……33

Chapter 5 Energy harvesting performance in linear shear flow……...36

5.1 Power efficiency and energy harvesting efficiency…….36

5.2 Mechanism of energy harvesting capacity enhancement…….40

Chapter 6 Energy harvesting performance in non-sinusoidal heaving motion……52

6.1 Power efficiency and energy harvesting efficiency…….52

6.2 Mechanism of energy harvesting capacity enhancement……56

Chapter 7 Conclusions ……..…..67

References ……..….69

LIST OF ABBREVIATIONS

LEVs	Leading edge vortices
AOA	Angle of Attack (AOA)
SIMPLE	Semi Implicit Method for Pressure-Linked Equations

LIST OF FIGURES

Figure 1.1: Design concept of Stingray (left) and bioSTREAM^{TM} (right). From A. westwood [22] and Biopower webpage [23] 5

Figure 2.1: Schematic of the flapping foil for energy harvesting 10

Figure 2.2: Variation of non sinusoidal heaving motions in one cycle. H1 and H2 have trapezoidal waveform and H3, H4, and H5 have triangular waveform.....11

Figure 2.3: Flow regimes of a flapping foil viewed in the reference frame moving with the free stream flow at U_∞: (a) energy extraction regime, (b) feathering regime, (c) propulsion regime. The motion of a foil is from right to left. From Kinsey & Dumas [14] 13

Figure 3.1: Spring-Based Smoothing on interior nodes: (a) start and (b) end. From FLUENT 12.1 theory guide [11] 23

Figure 3.2: Mechanism of sliding mesh on interface nodes: (a) start and (b) end. From FLUENT 12.1 theory guide [11] 24

Figure 3.3: Abnormal extended grid around a foil: (a) Before starting re-meshing, (b) Spring constant factor = 1, number of iteration = 10^5, convergence tolerance = 1×10^{-9}, and size re-meshing interval = 1, (c) Spring constant factor = 0, number of iteration = 9×10^5, convergence tolerance = 1×10^{-7}, and size re-meshing interval = 1, (d) Spring constant factor = 0, number of iteration = 5×10^5, convergence tolerance = 1×10^{-7}, and size re-meshing interval = 1 26

Figure 3.4: Comparison between (left column) vorticity filed by Guglielmini & Blondeaux [28] and (right column) numerical simulations by Dnamic & re-meshing mesh model about the flow field around a foil having heaving and pitching motion. The kinematic parameters are as follows: (a) St = 0.32, θ_0= 30, H_0= 0.75, ϕ= 90, (b) St = 0.32, θ_0= 30, H_0= 0.75, ϕ = 75, (c) St = 0.32, θ_0= 30, H_0= 0.75, ϕ = 105 27

Figure 3.5: (a) The computational domain of sliding mesh, (b) Close-up view of the rotating sub-domain, (c) Close-up view of the sliding interface, (c) Close-up view of computational mesh near the foil 29

Figure 3.6: (a) Vorticity filed from Kinsey & Dumas, (b) Current data by dynamic and re-meshing model, (c) Current data by sliding mesh model. The kinematic parameters are as follows: f^* = 0.14, θ_0= 76.33, H_0= 1 at t/T = 0.5 30

Figure 4.1: Energy harvesting efficiency as function of non-dimensional frequency. The kinematic parameters are as follows: θ_0= 75 deg, H_0/c= 1 at RE = 200 35

Figure 5.1: Three kinds of linear shear inlet flow that have different shear rate.....37

Figure 5.2: (a) Comparison of time-mean output power coefficient versus non-dimensional frequencies for different K, (b) Comparison of time-mean energy harvesting efficiency versus non-dimensional frequencies for different K.....39

Figure 5.3: Plots of lift coefficient (C_L), heaving velocity (dh/dt), momentum coefficient (C_M) and pitching velocity ($d\theta/dt$) in one cycle. (a - b) f^* = 0.14 in uniform flow, (c - d) f^* = 0.14 in linear shear flow (K = 0.1), (e - f) f^* = 0.14 in linear shear flow (K = 0.2), (g - h) f^* = 0.14 in linear shear flow (K = 0.3) 42

Figure 5.4: Plots of lift coefficient (C_L), heaving velocity (dh/dt), momentum coefficient (C_M) and pitching velocity ($d\theta/dt$) in one cycle. (a - b) f^* = 0.18 in uniform flow, (c - d) f^* = 0.18 in linear shear flow (K = 0.1), (e - f) f^* = 0.18 in linear shear flow (K = 0.2), (g - h) f^* = 0.18 in linear shear flow (K = 0.3) 44

Figure 5.5: Vorticity fields at f* of 0.14 in uniform inlet flow.....48

Figure 5.6: Vorticity fields at f* of 0.14 in linear shear flow (K = 0.2) 48

Figure 5.7: Vorticity fields at f* of 0.18 in uniform inlet flow.....49

Figure 5.8: Vorticity fields at f* of 0.18 in linear shear flow (K = 0.2) 49

Figure 5.9: Pressure fields at f* of 0.14 in uniform inlet flow.....50

Figure 5.10: Pressure fields at f* of 0.14 in linear shear flow (K = 0.2) 50

Figure 5.11: Pressure fields at f* of 0.18 in uniform inlet flow.....51

Figure 5.12: Pressure fields at f* of 0.18 in linear shear flow (K = 0.2) 51

Figure 6.1: (a) Comparison of time-mean output power coefficient versus non-dimensional frequencies for different *D* of trapezoidal heaving motion, (b) Comparison of time-mean energy harvesting efficiency versus non-dimensional frequencies for different *D* of trapezoidal heaving motion.....54

Figure 6.2: (a) Comparison of time-mean output power coefficient versus non-dimensional frequencies for different *G* of triangular heaving motion, (b) Comparison of time-mean energy harvesting efficiency versus non-dimensional frequencies for different *G* of triangular heaving motion.....55

Figure 6.3: Plots of lift coefficient (C_L), heaving velocity (*dh/dt*), momentum coefficient (C_M) and pitching velocity ($d\theta/dt$) in one cycle. (a - b) f^* = 0.15 in sinusoidal heaving motion, (c - d) f^* = 0.15 in H1 (*D* = 1.532), (e - f) f^* = 0.15 in H3 (*D* = 0.711) 58

Figure 6.4: Plots of lift coefficient (C_L), heaving velocity (*dh/dt*), momentum coefficient (C_M) and pitching velocity ($d\theta/dt$) in one cycle. (a - b) f^* = 0.15 in sinusoidal heaving motion, (c - d) f^* = 0.15 in H4 (*G* = 0.925), (e - f) f^* = 0.15 in H6 (*G* = 0.354) 59

Figure 6.5: Vorticity fields at f* of 0.15 in sinusoidal heaving motion.....61

Figure 6.6: Vorticity fields at f* of 0.15 in H1 (trapezoidal heaving motion) 62

Figure 6.7: Vorticity fields at f* of 0.15 in H3 (trapezoidal heaving motion) 62

Figure 6.8: Vorticity fields at f* of 0.15 in H4 (triangular heaving motion) 63

Figure 6.9: Vorticity fields at f* of 0.15 in H6 (triangular heaving motion) 63

Figure 6.10: Pressure fields at f* of 0.15 in sinusoidal heaving motion.....64

Figure 6.11: Pressure fields at f* of 0.15 in H1 (trapezoidal heaving motion) 64

Figure 6.12: Pressure fields at f* of 0.15 in H3 (trapezoidal heaving motion) 65

Figure 6.13: Pressure fields at f* of 0.15 in H4 (triangular heaving motion) 65

Figure 6.14: Pressure fields at f* of 0.15 in H6 (triangular heaving motion) 66

LIST OF TABLES

Table 2.1: Table of *D* and *G* value for non-sinusoidal heaving motion 12

Table 3.1: (a) Table of the number of grids, (b) Table of the time step, (c) Convergence of energy extraction efficiencies η with respect to the number of mesh grids and the time step. The kinematic parameters are as follows: $f^* = 0.14$, $\theta_0 = 76.33$, $H_0 = 1$ at Re=1100 31

Table 3.2: (a) Table of the number of grids, (b) Table of the time step, (c) Convergence of energy extraction efficiencies η with respect to the number of mesh grids and the time step. The kinematic parameters are as follows: $f^* = 0.14$, $\theta_0 = 76.33$, $H_0 = 1$ at $t/T = 0.5$ 31

ACKNOWLEDGEMENTS

Foremost, I would like to gratefully acknowledge Professor Qiang Zhu for his support. His continuing guidance, patience, enthusiasm, and encouragement helped me in all the research and writing of thesis. I could not have imagined having a better advisor and mentor for my MS study. Also I gave special thanks to Professor Alison L. Marsden and Professor Eric Lauga for their support as the chair of my committee and co-advisor, respectively. Their all advices and immense knowledge motivated me a lot to study in Fluid Mechanics.

I would also like to thank to Zhangli Peng, Kourosh Shoele, and Sara Salehyar for their help on data collection and information. I owe my deepest gratitude to all lab members.

My sincere thanks also go to my friends: Daeyup David Han, Taeseok Oh, Kilhyun Bang, Jihyun Kim, Seungmin Lee, Yoona Kim and other UCSD friends for always helping me by giving me friendship and cheering me a lot.

My deepest gratitude goes to my family: my lover Seojung Claire Youn who have always been there with me and giving me joy, supportive and happiness, my sister Miyoung who has always been affectionate, my beloved grandfather Joosang Cho for his bondless love, and last but not least my parents Hangmin Cho and Sunhee Ga for their loving consideration and understanding and so much more.

ABSTRACT OF THE THESIS

Analysis of a Flapping Foil System for Energy Harvesting at low Reynolds number

by

Hunkee Cho

Master of Science in Engineering Sciences (Mechanical Engineering)

University of California, San Diego, 2011

Professor Alison L. Marsden, Chair

The new type of power generation system which mimics the flapping motion of insects or fish has been studied in recent years. The biological flapping foil is capable of harvesting energy from incoming wind or current. A non-sinusoidal trajectory profile and linear shear inlet profile are proposed for the flapping foil in the energy harvesters instead of conventional sinusoidal plunging and pitching motions to get better energy harvesting performance. In this study we create a numerical model using the commercial finite volume computational fluid dynamics code FLUENT to investigate the energy harvesting performance of such a system. We control linear shear inlet profiles and non-sinusoidal profiles by varying parameters *K*, *D*, and *G*. This investigation shows that using a linear

shear inlet profile and a non-sinusoidal heaving profile may increase energy harvesting efficiency as high as 9% and 3% compared to conventional flapping foil systems, respectively. Specifically, staying leading edge vortex on the upper surface of a foil and synchronization between the foil movements and the evolution of vorticity field is crucial points to get higher energy harvesting efficiency. Controlled these will be able to enhance the energy harvesting capacity.

Chapter 1

INTRODUCTION

1.1 Motivation and Goals

Bio-inspired flapping wing systems have been a very active area of research in recent years. Insect flight, fish locomotion, and harmonically flapping foils provide particularly interesting examples of such systems. Flapping wing systems have similar physical phenomena and flow separation in specific region. A variation of the effective angle of attack and the Reynolds number by wing chord length and flapping frequency leads to the change of the leading edge vortices (LEVs) and span-wise flow structures which influences the aerodynamic force generation. Flapping wings with appropriate wing kinematics, flapping frequencies, and wing shapes can enhance lift and thrust by exploiting vortical flows around flapping wings under a number of conditions (W. Shyy *et al.* [1], Anderson *et al.* [2], Triantafyllou *et al.* [3], Wang [4], Liu *et al.* [5], Rammamutri & Sandberg [6]). Especially, fish locomotion has admirable hydrodynamic performance with higher propulsion efficiency and low drag by extracting energy through the flapping motion of fin (Zhu *et al.* [7], Liao *et al.* [8]). In the field of engineering and fluid mechanics, the new type of power generation system which mimics insect flight or fish motion has been studied in recent years. The fundamental principle of this system depends on fluid-induced vibrations from an oscillating current or the wave-generated flow. After discovering the possibility of extract kinetic energy, this power generation

system has the potential to solve environmental issues of conventional turbines such as the horizontal axis rotor turbines and energy crisis in the fields of wind and tidal energy. The flapping foil systems have a number of advantages compared with conventional rotor blade systems. These systems have simpler structures and are easier to install in shallow water sites than conventional windmills or hydro-turbines. Most of all, having less noise than rotor blades and no large blade structures diminish negative impact on the environment. However, the commercialization of flapping foil systems for energy harvester has the difficulties because of nonlinear dynamics of vortex structures induced by boundary layer separation at the surface of foil and a bunch of controlling parameters such as pitching amplitude, heaving amplitude, flapping frequency and so on. Therefore, a thorough analysis is needed to determine characteristics of flapping foil systems and function from which man-made applications could benefit.

The main goal of this work is not to test the performance of real flapping foil systems in higher Reynolds numbers but to investigate the energy harvesting capacity of flapping foil systems and factors for the maximum efficiency of power extraction. The recent results of 2D simulation from Zhu [9] showed that the energy harvesting capacity of the flapping foil increases with Reynolds number. Furthermore, the higher Reynolds numbers system requires a bunch of grid and smaller grid size around foil to capture the boundary layer effect. Consequently, this will dramatically occur to increase the computational cost and effort. Current work will thus study the physical mechanism that affects energy extraction process in relatively low Reynolds numbers ($\sim O(10^2)$).

Here, we will focus on the simple symmetric flapping foil in a prescribed motion as models of insect flight or underwater swimmers. In particular, we will also investigate

what the benefits are of non-uniform incoming flow and non-sinusoidal heaving motion, for maximizing the efficiency of power extraction achieved by using commercial code FLUENT 12.1. In order to separate the effects of the effects of flexibility, we will conduct numerical analysis using a rigid foil. Future work may look to include flexibility as a parameter. Previous experimental and numerical work has been done to characterize the wakes of flapping foil systems restricted by considering simplified kinetic models or simplified environmental circumstances of flows.

1.2 Previous Work

The idea of flapping wing systems for harvesting energy in uniform flows initially was suggested by McKinney & Murakami [12] in 1981. Their prototype combined pitching and plunging motions extracted power from air flows and maximum power efficiency of this system was 16.8% at pitching amplitude of 30 degrees and phase angle of 90 degrees. This efficiency was comparable to that of the conventional windmill. In particular, Jones & Platzer [13] carried out. Their extensive computation results showed foil combined pitching and plunging motions could be used as both a propulsive device and as a power-extraction device. It was found that energy transfer from the flow to foil if the pitching amplitude was increased to a sufficiently high value. Recent studies concentrated on flow-body interaction systems that extract energy from the vortices induced flapping foils which was activated in uniform flow. This system is called an activated system and the motion of foil is prescribed by pitching motion and heaving motion. Many researchers (Kinsey & Dumas [14]; Zhu et al. [15]; Zhu & Peng [16]) have used this system for getting feasible ways for maximum efficiency of energy harvesting.

Kinsey & Dumas [14] presented a mapping of energy harvesting efficiency of oscillating NACA0015 airfoil as a function of non-dimensional frequency from 0 to 0.25 and pitching amplitude from 0 degree to 90degrees. They made lots of combination of these parameters and got maximum power harvesting efficiency of 34% at pitching amplitude of 75 degrees and incoming flow velocity of around 0.15 through unsteady laminar flow numerical analysis by using the commercial code FLUENT 6.1. Zhu et al. [15] investigated the performance of flapping foils as a new type of energy harvester through numerical modeling by using two methods, a 2D thin-plate model and a 3D nonlinear boundary-element model. They examined the energy extraction capacity and efficiency of this system at various geometric, mechanical, and kinematic parameters and found the optimal parameters for enhancing the performance. Moreover, they found that the performance could be enhanced by the presence of a solid ground and the thickness of the foil. A numerical model based on the Navier-Stokes equations by Zhu & Peng [16] was made to study the performance of flapping foil system in low Reynolds numbers. They showed that energy of the leading-edge vortices could be redeemed to improve the power extraction capacity through vortex-body interactions. On the other hand, purely passive system by Peng & Zhu [17] was attempted to reduce the complexity of design of an activated system. One of modes of purely passive system such as pitching motion was prescribed and heaving motion was induced by unsteady flow instability for utilizing power extraction. Through this passive system, they decided combinations of geometric and mechanical parameters to get the feasibility of stable flow power extraction. In the subsequent work by Zhu [9], numerical model using Navier-Stokes algorithm and Orr-Sommerfeld equation was shown the relation between wake stability and the power

harvesting efficiency. Kinsey & Dumas [14] performed lots of parametric studies for getting higher energy extraction efficiency, but they didn't explain why there exists an optimal frequency. They suggested that energy efficiency is related to evolution of wake. The wake is unstable and the frequency of the most unstable mode would be indicated. He found that this frequency of unstable mode is identical to that of the highest energy extraction efficiency. For finding the feasible ways to get higher energy extraction efficiency, non-sinusoidal motion like square wave motion is adopted to heaving motion by M. F. Platzer et al. [18, 19]. They struggled to find effective motion control by changing rapid rotation velocity during stroke reverse. Qing Xiao et al. [20, 21] also used non-sinusoidal motion like trapezoidal wave motion for prescribing pitching motion for enhancing energy extraction performance. These recent studies showed that non-sinusoidal motion could be optimal foil motion that increases the total output efficiency. In recent years, Engineering Business and BioPower have been developing tidal stream generation technology. In 2002, Engineering Business Ltd. designed, built and installed the first full scale tidal stream generator which is the 150 kW Stingray demonstrator. BioPower has developed 250kW bioSTREAM^{TM} which has bio-inspired design for enegy conversion since 2006 [22, 23].

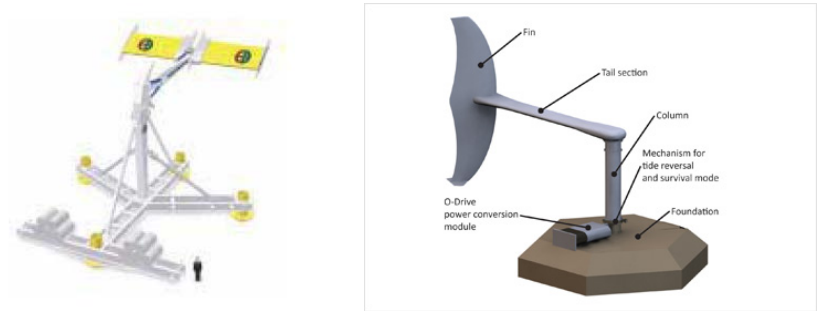

Figure 1.1: Design concept of Stingray (left) and bioSTREAM^{TM} (right). From A. westwood [22] and Biopower webpage [23]

1.3 Approach and Objectives

In the course of this work, numerical simulations are performed with Eulerian approach using dynamics mesh technique as a tool for vortex analysis of a flapping foil. We use GAMBIT 2.3 [10] to make geometry and to form moving grid and boundary conditions. Commercial code FLUENT 12.1[11] are used for investigate flow physics and wake around moving foil. Accuracy of this numerical simulation is validated through a rigorous validation includes spatial and temporal convergence tests as well as comparisons with previous work.

The prescribed motion of previous studies of flapping foil systems is mostly sinusoidal heaving/pitching and it is one of simple harmonic profiles. The interesting characteristic of propulsion flapping foil by previous research [2, 20, 21, 24] was found that the rising-up trend for thrust coefficient and input power coefficient are no longer exists and diminish quickly at higher Strouhal number. The main reason of this phenomenon is related to a decrease in effective angle of attack at higher Strouhal number. The better propulsion performance was shown at certain maximum effective angle of attack and the derived heaving motion in this case is not sinusoidal heaving motion but non-sinusoidal heaving motion. In addition, the inlet flow of previous studies [9, 12-21, 24] is set as mainly uniform flow. This incoming flow profile is not easy to stay on all the time and non-uniform incoming flow can change the effective angle of attack. This parameter also has the possibility to make better performance of flapping foil too. To test diverse circumstance of flapping foil and to enhance the power extraction performance is need to test non-incoming flow conditions. Such these characteristics

motivate us to investigate whether the energy extraction efficiency of flapping foil can be enhanced by non-sinusoidal oscillations and non-uniform incoming flows.

In the present work, non-sinusoidal trajectories are constructed by two types of wave motion such as triangular heaving motion and trapezoidal heaving motion. Berman and Wang [25] found the optimal wing kinematics of each insect to minimize energy consumption in hovering flight. We adopted these optimal wing trajectories and curve-fitting insect wing kinematics for making triangular heaving motion and trapezoidal heaving motion [26]. There are many kinds of inlet flow profile but we simplified these profiles. Non-uniform flow that we used is thus linear shear inlet flow. We turned shear rate as three types to change the inlet flow profiles.

This study is therefore focused on how motion trajectory and inlet flow profiles can affect energy extraction performance. A mapping of energy extraction efficiency is presented for a given single foil geometry, a fixed Reynolds number, a fixed heaving amplitude, a fixed pitching amplitude, and a fixed pitching axis location to concentrate parameters that were mentioned above.

1.4 Overview

- In Chapter 2, we review the concept and fundamentals of the flapping foil systems. This chapter contains details of flapping foil motion that is prescribed. Operating regimes that have two different regimes and energy extraction will be explained.

- Chapter 3 contains details of the computational setup and techniques used in the course of the current work. We review the concept and definition of the Dynamic and re-meshing technique and the Sliding mesh technique. The merits of the Sliding mesh technique, as opposed to the Dynamic and re-meshing technique partially, are faster computational speed and higher accuracy result compared with Dynamic and re-meshing technique.

- In Chapter 4, 5 and 6, we report the results from cases of uniform flow on rigid single foil. Interpretation of this data led us to propose a new control parameter. Also we investigate the characteristics of linear shear flows and non-sinusoidal heaving motion from the optimization of insect wing trajectories.

- A discussion of the results, concluding remarks, and plans for future work are given in Chapter 7.

Chapter 2

FUNDAMENTALS OF FLAPPING FOIL SYSTEMS

2.1 The kinematics of a flapping foil

Nomenclature, equations, and explanation of the term used in equations in this section are based on Kinsey & Dumas's paper [14]. Basic flapping foil experiences simultaneous pitching and heaving motion as shown in Fig. 1.1. The foil motion can be written as follow.

$$\theta(t) = \theta_0 sin(\gamma t + \phi), \ \ \Omega(t) = \theta_0 \gamma cos(\gamma t + \phi) \tag{2.1}$$

$$h(t) = H_0 sin(\gamma t), \ \ V_y(t) = H_0 \gamma cos(\gamma t) \tag{2.2}$$

Where θ_0 is the pitching amplitude; H_0 is the heaving amplitude; Ω is the pitching velocity; V_y is the heaving velocity; γ is the angular frequency$(2\pi f)$; and ϕ is the phase angle between pitching motion and heaving motion. In this study, phase angle is kept constant at 90 degrees for harmonically symmetric foil motion and phase angle of 90 degrees is the best effective phase angle in flapping motion from previous study [14]. The free stream velocity of flapping foil is expressed as U_∞. The location of pitching axis is at position x_p on the foil chord line from the leading edge and is restricted to 1/3. It is also shown the best performance in previous results [14]. The geometry of a foil is identical to the NACA0015 foil.

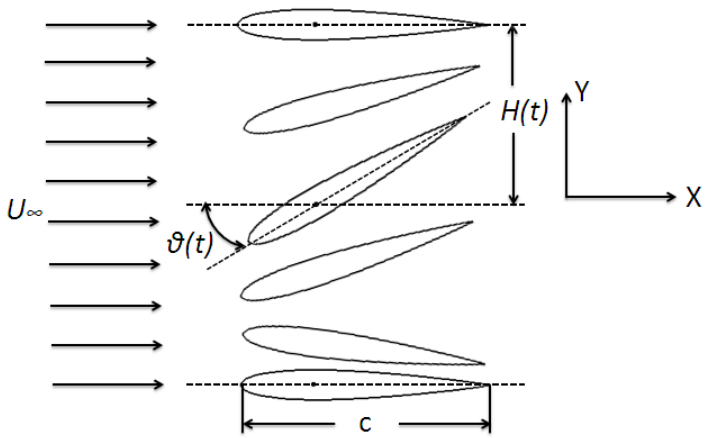

Figure 2.1: Schematic of the flapping foil for energy harvesting

Non sinusoidal heaving motions are composed of two different types of waveform: trapezoidal waveform and triangular waveform. These waveforms are inspired by results of the kinematics of insect wing for energy conservation [25, 26]. Berman and Wang [25] found the optimal kinematic for minimizing energy consumption of three kinds of insect wing. Dickinson *et al.* [26] studied wing rotation and aerodynamic basis of insect flight by using robotic experiments. They used simplified kinematics of the wing motion of fruit fly to better controlling robotic arm. We made non sinusoidal heaving motions based on these previous insect flight studies. The variation of non-sinusoidal heaving motion at different *D* and *G* over one cycle is shown in Figure 2.2.

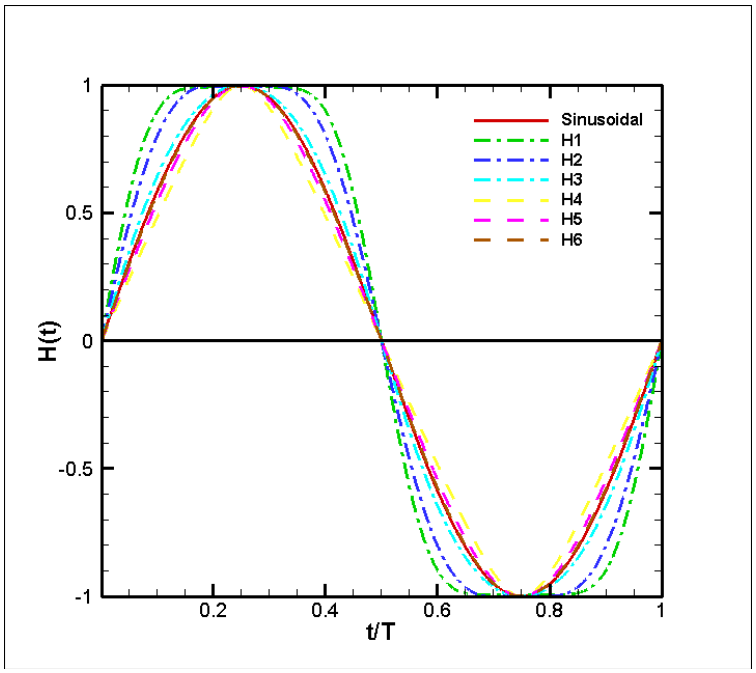

Figure 2.2: Variation of non sinusoidal heaving motions in one cycle. H1, H2, and H3 have trapezoidal waveform and H4, H5, and H6 have triangular waveform.

Trapezoidal heaving motions, $\mathrm{H_{N1}(t)}$, is given by a smoothed rectangular waveform,

$$H_{N1}(t) = \frac{1}{\tanh D} \tan[D \sin(2\pi f t)] \tag{2.3}$$

When D approaches ∞, $\mathrm{H_{N2}(t)}$ tends toward a rectangular waveform. If D approaches 0, $\mathrm{H_{N1}(t)}$ becomes a sinusoidal. On the other hand, Triangular heaving motions, $\mathrm{H_{N2}(t)}$, is given by a smoothed triangular waveform,

$$H_{N2}(t) = \frac{0.636(\pi/2)}{\sin^{-1} G} \sin^{-1}[G \sin(2\pi f t)] \tag{2.4}$$

where $0 < G < 1$. When G approaches 1, $H_{N2}(t)$ becomes a triangular waveform. If G approaches 0, $H_{N2}(t)$ will be a sinusoidal. Hence, in effect, the value of D and G is related to the duration of the foil heaving reversal. As seen from Table 2.1, there are 6 values of D and G which need to describe the heaving motion of a flapping foil in (2.3)

and (2.4). We adopted the values of *D* and *G* from results of Berman and Wang [25] and tried to modify some of these values for achieving higher power extraction efficiency. In other words, we used these values from previous results [25] directly in cases of H3, H4, and H5. Meanwhile, we revised *D* and *G* value in cases of H1, H2, and H6 for highlighting characteristics of non-sinusoidal heaving motion and find the best pathway for higher energy extraction efficiency.

Table 2.1: Table of *D* and *G* value for non-sinusoidal heaving motion

Type	Description	D or G value
H1	Smoothed rectangular waveform	2.015
H2	Smoothed rectangular waveform	1.532
H3	Smoothed rectangular waveform	0.711
H4	Smoothed triangular waveform	0.925
H5	Smoothed triangular waveform	0.704
H6	Smoothed triangular waveform	0.354

2.2 Energy extraction regime

There are two kinds of operating flow regime based on the prescribed motion of flapping foil and free stream flow conditions: power extraction and propulsion. These flow regimes are distinct by the direction of aerodynamic forces generated by flapping foil. For qualifying the effect of prescribed motion, it is important to define a feathering parameter. A feathering parameter can play a major role in distinguishing the two regimes and can be expressed as follow.

$$\chi = \frac{\theta_0}{arctan\left(\frac{H_0 \gamma}{U_\infty}\right)} \tag{2.5}$$

If a feathering parameter, χ is bigger than 1, the flow past foil is power extraction regime, whereas if a feathering parameter χ is smaller than 1, the flow past foil is propulsion regime. When χ is 1, it is called feathering regime (no power extraction and no propulsion). These flow regimes are shown in the schematic representation of Figure 2.3.

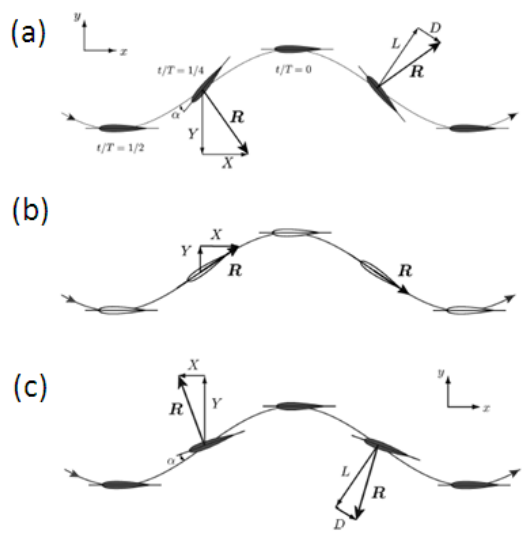

Figure 2.3: Flow regimes of a flapping foil viewed in the reference frame moving with the free stream flow at U_∞: (a) energy extraction regime, (b) feathering regime, (c) propulsion regime. The motion of a foil is from right to left. From Kinsey & Dumas [14]

The resultant force is decomposed into vertical and horizontal forces of a flapping foil. In energy extraction regime (see Figure 2.3 (a)), the direction of resultant force is identical to that of vertical force. As a result, the flow past a flapping foil would generate a positive work on a foil. Thus, the flapping foil system can get extraction energy as long as the direction of horizontal force is positive. In propulsion regime, the direction of resultant force is opposite to the vertical force. It causes that flapping foil

system has to do some work on the fluid. The feathering parameter is based on the maximum effective angle of attack α_{max} and the maximum effective velocity V_{max}. Effective angle of attack α_{eff} is crucial point to quantify the effect of combination of pitching and heaving in a flapping foil problem. These values can be written as follow.

$$\alpha_{max} = \left| arctan\left(\frac{H_0\gamma}{U_\infty}\right) - \theta_0 \right| \tag{2.6}$$

$$V_{max} = \sqrt{{U_\infty}^2 + (H_0\gamma)^2} \tag{2.7}$$

2.3 Extracted power and the power harvesting efficiency

To quantify energy harvesting, the time-mean extracted power is defined as integrating the instantaneous power extracted in one cycle. The instantaneous power extracted is composed of the combination of a the instant total power of heaving motion $P_y(t) = Y(t)V_y(t)$ and the instant total power of pitching $P_\theta(t) = M(t)\Omega(t)$, where $Y(t)$ is vertical component of aerodynamic force $V_y(t)$ is instance heaving velocity; $M(t)$is the torque about the pitching axis x_p. The instance power extraction and the time-mean extract power can be expressed as follow.

$$P = Y(t)\frac{dh(t)}{dt} + M(t)\frac{d\theta(t)}{dt} \tag{2.8}$$

$$\bar{P} = \frac{1}{T}\int_0^T P dt \tag{2.9}$$

The non-dimensional instantaneous power coefficient is defined as follow.

$$C_p = \frac{P}{\frac{1}{2}\rho U_\infty^3 c} = \frac{2}{\rho U_\infty^3 c}\left[Y(t)\frac{dh(t)}{dt} + M(t)\frac{d\theta(t)}{dt}\right] = \frac{1}{U_\infty}\left[C_L(t)\frac{dh(t)}{dt} + C_M(t)\frac{d\theta(t)}{dt}\right] \tag{2.10}$$

where $C_L(t)$ is the instantaneous lift coefficient and $C_M(t)$ is the instantaneous momentum coefficient. These coefficients can be expressed as follow.

$$C_L(t) = \frac{Y(t)}{\frac{1}{2}\rho U_\infty^2 c} \tag{2.11}$$

$$C_M(t) = \frac{M(t)}{\frac{1}{2}\rho U_\infty^2 c} \tag{2.12}$$

Thus, the time-mean extracted power in one cycle can be calculated and its non-dimensional form can be expressed as follow.

$$\overline{C_p} = \frac{1}{T}\int_0^T C_p dt = \frac{\bar{P}}{\frac{1}{2}\rho U_\infty^3 c} \tag{2.13}$$

$$\overline{C_p} = \overline{C_{P_y}} + \overline{C_{P_\theta}} = \frac{1}{U_\infty T}\left[\int_0^T C_L(t)\frac{dh(t)}{dt} + C_M(t)\frac{d\theta(t)}{dt}\right] \tag{2.14}$$

or

$$\overline{C_p} = \overline{C_{P_y}} + \overline{C_{P_\theta}} = \int_0^1 \left\{C_Y(t)\frac{V_y(t)}{U_\infty} + C_M(t)\frac{\Omega(t)c}{U_\infty}\right\} d\left(\frac{t}{T}\right) \tag{2.15}$$

The power harvesting efficiency can be induced from the time-mean extracted power. It is represented as the ratio of the total extracted power to the total incoming flow energy flux within the swept area.

$$\eta = \frac{\bar{P}}{\frac{1}{2}\rho U_\infty^3 d} = \frac{\overline{P_y} + \overline{P_\theta}}{\frac{1}{2}\rho U_\infty^3 d} = \frac{\overline{C_P}\frac{1}{2}\rho U_\infty^3 c}{\frac{1}{2}\rho U_\infty^3 d} = \overline{C_p}\frac{c}{d} \tag{2.16}$$

Where ρ is the density of fluid; c is the wing chord length; d is the overall vertical extent of the foil motion. Energy harvesting efficiency is defined as the portion of flow energy flux within the swept area extracted by the system. For reference, the maximum energy extraction efficiency is theoretically known as 59% from the result of Betz [27] analysis

of a stationary inviscid stream tube around a energy-extraction device.

Chapter 3

NUMERICAL METHOD

3.1 Governing equations

In this study, numerical analysis was conducted by commercial code FLUENT 12.1. GAMBIT 2.3 which is the one of pre-processing programs of FLUENT 12.1 was used for forming foil geometry and grid. For prescribing the motion of the foil, Dynamic and re-meshing technique that redeploy the position of node at each time step for describing rigid body motion was used in this code solver. The main properties of flow in this study were assumed by incompressible, viscid, and laminar flow. Two dimensional incompressible and unsteady Navier-Stokes equations in Cartesian coordinates were used for solving numerically lots of cases that have the pitching and heaving motion of the foil in this study. The numerical method of FLUENT 12.1 was mentioned above simply.

Continuity equation

$$\frac{\partial u}{\partial x} + \frac{\partial v}{\partial y} + \frac{\partial w}{\partial z} = 0 \tag{3.1}$$

Momentum equations

$$\frac{\partial u}{\partial t} + u\frac{\partial u}{\partial x} + v\frac{\partial u}{\partial y} + w\frac{\partial u}{\partial z} = -\frac{\partial p}{\partial x} + \frac{1}{Re}\left(\frac{\partial^2 u}{\partial x^2} + \frac{\partial^2 u}{\partial y^2} + \frac{\partial^2 u}{\partial z^2}\right) \tag{3.2}$$

$$\frac{\partial v}{\partial t} + u\frac{\partial v}{\partial x} + v\frac{\partial v}{\partial y} + w\frac{\partial v}{\partial z} = -\frac{\partial p}{\partial y} + \frac{1}{Re}\left(\frac{\partial^2 v}{\partial x^2} + \frac{\partial^2 v}{\partial y^2} + \frac{\partial^2 v}{\partial z^2}\right) \tag{3.3}$$

$$\frac{\partial w}{\partial t} + u\frac{\partial w}{\partial x} + v\frac{\partial w}{\partial y} + w\frac{\partial w}{\partial z} = -\frac{\partial p}{\partial y} + \frac{1}{Re}\left(\frac{\partial^2 w}{\partial x^2} + \frac{\partial^2 w}{\partial y^2} + \frac{\partial^2 w}{\partial z^2}\right) \tag{3.4}$$

where u, v, and w are linear velocity in Cartesian coordinates respectively, and p is

pressure. The fluid module implements the Navier-Stokes equations (equation (3.2), (3.3) and (3.4)) using the finite volume method, a segregated approach, the SIMPLE algorithm, and an arbitrary Lagrangian-Eulerian formulation.

To determine the minimum grid size, two dimensional Navier-Stokes model reported by Guglielmini & Blondeaux [28] was applied. A reference Cartesian frame moves with the foil to new Cartesian coordinates. The foil by considering a Joukowski profile can be mapped into a circle of radius ($\lambda^* + e^* + s^*$) using that transformation.

$$(X^*, Y^*) = (\xi^*, \eta^*) + \lambda^{*2} \frac{(\xi^* - e^*, -\eta^*)}{(\xi^* - e^*)^2 + \eta^{*2}} + (\xi^* - e^*, 0) \tag{3.5}$$

The governing equation will be changed to

$$\frac{\partial \omega}{\partial t} + \frac{\hat{A}}{\sqrt{J}}\left[v_r \frac{\partial \omega}{\partial r} + \frac{v_\theta}{r}\frac{\partial \omega}{\partial \theta}\right] = \frac{\hat{A}}{ReJ}\left[\frac{\partial^2 \omega}{\partial r^2} + \frac{1}{r}\frac{\partial \omega}{\partial r} + \frac{1}{r^2}\frac{\partial^2 \omega}{\partial \theta^2}\right] \tag{3.6}$$

$$\frac{\partial^2 \psi}{\partial r^2} + \frac{1}{r}\frac{\partial \psi}{\partial r} + \frac{1}{r^2}\frac{\partial^2 \psi}{\partial \theta^2} = -J\omega \tag{3.7}$$

And, dimensionless variables are defined as following.

$$t = t^* \sigma^*,\ r = \frac{r^*}{\lambda^*},\ (\xi, \eta) = \frac{(\xi^*, \eta^*)}{\lambda^*},\ \psi = \frac{\psi^*}{\hat{A}\sigma^*\ \lambda^*} \tag{3.8}$$

$$\omega = \frac{\omega^* \lambda^*}{\widehat{A^*}\ \sigma^*},\ A = \frac{A^*}{\lambda^*}, Re = \frac{\widehat{A^*}\ \sigma^* \lambda^*}{\upsilon^*}, \hat{A} = \frac{\widehat{A^*}}{\lambda^*} \tag{3.9}$$

$$J = 1 + \frac{1 - 2[(\xi - e)^2 + \eta^2]}{[(\xi - e)^2 + \eta^2]^2} \tag{3.10}$$

where J is the Jacobian transformation. From above equations, the grid size near the foil is always smaller than $0.1\min\left(\sqrt{\frac{2\upsilon^*}{\sigma^*}}, \sqrt{\frac{4\upsilon^*\lambda^*}{U_0^*}}\right)$, where $\sqrt{\frac{2\upsilon^*}{\sigma^*}}$ and $\sqrt{\frac{4\upsilon^*\lambda^*}{U_0^*}}$ are the approximate thickness of the Stokes and Blasius boundary layer respectively. The exact expression and explanation of these equations can be found in Guglielmini & Blondeaux [28].

3.2 The theory of deforming and sliding meshes

It is impossible to use conventional steady flow solver method if the shape of the domain is changing with time due to pitching and heaving motion on the boundaries. To break this limitation, FLUENT 12.1 supports dynamic & auto re-meshing and sliding mesh techniques for describing moving boundaries in model flows. Dynamic mesh technique can change the position of nodes and the shape of grid near moving rigid bodies at each time step. Auto re-meshing technique is used for the update of the mesh at each time step based on the new positions of the domain boundaries. Sliding mesh technique used two or more cell zones. Each cell zone is bounded by at least one interface boundary condition where it meets the opposing cell zone. The motion of foil can be described by using User-Defined Functions (UDFs) is a kind of sub-routines written in C++.

3.2.1 Conservation equations

In dynamic mesh scheme, the integral form of the conservation equation for a general scalar (ϕ) on an arbitrary control volume (V) which boundaries is moving can be written as

$$\frac{d}{dt}\int_V \rho\phi dV + \int_{\partial V}\rho\phi\left(\vec{u} - \overrightarrow{u_g}\right)\cdot d\vec{A} = \int_{\partial V}\Gamma\nabla\phi\cdot d\vec{A} + \int_V S_\phi dV \qquad (3.11)$$

where ρ is the fluid density, $\vec{u}$ is the flow velocity vector, $\overrightarrow{u_g}$ is the grid velocity of the moving mesh, Γ is the diffusion coefficient, S_ϕ is the source term of ϕ.

∂V is used to represent the boundary of the control volume V. The time derivative term in Equation (3.11) can be written as by using a first-order backward difference formula.

$$\frac{\mathrm{d}}{\mathrm{dt}} \int_{\mathrm{V}} \rho\phi \mathrm{dV} = \frac{(\rho\phi\mathrm{V})^{\mathrm{n}+1} - (\rho\phi\mathrm{V})^{\mathrm{n}}}{\Delta\mathrm{t}} \tag{3.12}$$

where n and $n+1$ mean the each quantity at the current and next time level. The volume $\mathrm{V}^{\mathrm{n}+1}$ at $n+1$ th time level is calculated from

$$\mathrm{V}^{\mathrm{n}+1} = \mathrm{V}^{\mathrm{n}} + \frac{\mathrm{dV}}{\mathrm{dt}} \Delta\mathrm{t} \tag{3.13}$$

where $\frac{dV}{dt}$ is the volume time derivative of the each control volume. For satisfying the grid conservation law, the volume time derivative of the each control volume is computed from

$$\frac{\mathrm{dV}}{\mathrm{dt}} = \int_{\partial\mathrm{V}} \overrightarrow{\mathrm{u_g}} \cdot \mathrm{d}\overrightarrow{\mathrm{A}} = \sum_{\mathrm{j}}^{\mathrm{n_f}} \overrightarrow{\mathrm{u_{g,j}}} \cdot \overrightarrow{\mathrm{A_j}} \tag{3.14}$$

where n_f is the number of faces on the control volume and A_j is the j face area vector. The $\overrightarrow{u_{g,j}} \cdot \overrightarrow{A_j}$ on each control volume face is calculated from

$$\overrightarrow{u_{g,j}} \cdot \overrightarrow{A_j} = \frac{\partial V_j}{\Delta t} \tag{3.15}$$

where ∂V_j is the volume swept out by the control volume face j over the time step Δt.

In the sliding mesh scheme, the motion of moving zones is tracked relative to the fixed frame. Thus, if no moving reference frames are attached to the computational domain, it is simplified that the fluid mass flux can transfer across the interfaces. In the sliding mesh formulation, the control volume remains constant. From Equation (3.13), $\frac{dV}{dt} = 0$ and $V^{n+1} = V^{n}$. Therefore, Equation (3.12) can be expressed as follows:

$$\frac{d}{dt}\int_V \rho\phi dV = \frac{[(\rho\phi)^{n+1}-(\rho\phi)^n]V}{\Delta t} \tag{3.16}$$

3.2.2 Dynamic mesh theory

There are three groups of mesh motion methods in FLUENT to be available to update the volume mesh in the deforming regions subject to the motion defined at the boundaries: smoothing methods, dynamic layering, local re-meshing methods. Using structure mesh is difficult to conduct numerical analysis because of the complexity of foil kinematic that is the combination of heaving and pitching motion. Thus, we used unstructured mesh in this study and selected smoothing methods and local re-meshing methods for using dynamic mesh strategy. It is able to use dynamic layering method in structure mesh. The edges between any two mesh nodes are idealized as a network of interconnected springs in the spring-based smoothing method. The initial spaces of the edges before moving by motion description maintain the equilibrium state of the mesh. A displacement by motion description at a given boundary node will generate a force proportional to the displacement along all the springs connected to the node. Using Hooke's Law, the force on a node can be expressed as

$$\vec{F_i} = \sum_j^{n_i} k_{ij}\left(\Delta\vec{x_j} - \Delta\vec{x_i}\right) \tag{3.17}$$

where $\Delta\vec{x_i}$ and $\Delta\vec{x_j}$ are the displacements of node *i* and its neighbor *j*, n_i is the number of neighboring nodes connected to node *i*, and k_{ij} is the spring constant between node *i* and node *j*. The spring constant, k_{ij} is defined as

$$k_{ij} = \frac{1}{\sqrt{|\Delta\overrightarrow{x_i} - \Delta\overrightarrow{x_j}|}} \tag{3.18}$$

The net force on a node due to connected springs should be zero at equilibrium state. For such a reason, iterative equation should be expressed as

$$\Delta x_i^{m+1} = \frac{\sum_j^{n_i} k_{ij}\, \Delta x_i^m}{\sum_j^{n_i} k_{ij}} \tag{3.19}$$

Equation (3.19) can be solved using a Jacobi sweep on all interior nodes because boundary node positions have been updated. At convergence state, the positions of boundary are updated such that

$$\vec{x}_i^{n+1} = \vec{x}_i^n + \Delta\vec{x}_i^{m,converged} \tag{3.20}$$

where *n+1* and *n* are expressed as the positions at the next time step and the current time step, respectively. The spring-based smoothing for a cylindrical cell zone where one end of the cylinder is moving is shown in Figures 3.1.

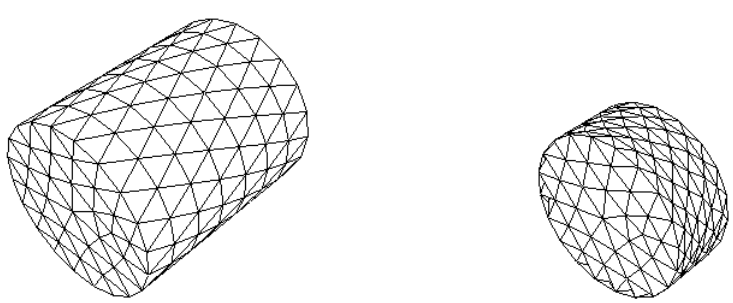

(a) (b)

Figure 3.1: Spring-Based Smoothing on interior nodes: (a) start and (b) end. From FLUENT 12.1 theory guide [11]

To use the local re-meshing method, cell skewness and minimum and maximum length scales is necessary to set up. FLUENT also support an optional sizing function for precisely controlling re-meshing. FLUENT evaluates each cell and marks it for re-meshing if it meets the following criteria:

1. It has a skewness that is greater than a specified maximum skewness.
2. It is smaller than a specified minimum length scale.
3. It is larger than a specified maximum length scale.

The exact expression and explanation of these equations can be found in FLUENT 12.1 theory guide [11]. The motion of foil can be described by using User-Defined Functions (UDFs) written in C++. FLUENT support many kind of UDF macros for changing parameters in subroutine or expressing special motion description. We used DEFINE_CG _MOTION that use to impose rigid body motion (translation or roation) to prescribe the motion of a foil.

3.2.3 Sliding mesh theory

We have to use the sliding mesh model to compute the unsteady flow field for getting a time-accurate solution for rotor-stator interaction rather than a time-averaged solution. The sliding mesh model is the most accurate method for simulating flows in multiple moving reference frames in FLUENT. The sliding mesh model permits motion multiple domains sliding relative to one another along interface boundaries. The unsteady solution that is sought in a sliding mesh simulation is time-periodic. That is, the unsteady

solution repeats with a period related to the speeds of the moving domains. Sliding mesh model can be applied to the numerical analysis of mixing tanks, rotor-stator interaction, vehicles in tunnels. There are two main mechanism of sliding mesh model. The governing equations are solved in their inertial reference frame for absolute quantities (e.g., absolute velocities). As seen in Figure 3.2, the meshes are moved and the fluxes at the sliding interfaces are recomputed for each time step.

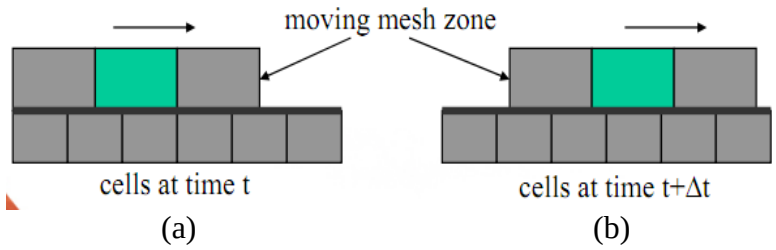

Figure 3.2: Mechanism of sliding mesh on interface nodes: (a) start and (b) end. From FLUENT 12.1 theory guide [11]

There is no interaction between stationary and moving parts. The interface boundary conditions of adjacent cell zones are associated with one another to form a grid interface. The two cell zones will move relative to each other along the grid interface. The motion of foil that was prescribed by specifying the linear and angular velocities about the center of gravity of a rigid body with time is determined based on the solution at each time step. We used DEFINE_ADJUST to prescribe the motion of a foil. DEFINE_ADJUST is a general macro that can be used to adjust or modify flow variables such as velocities or pressure in FLUENT that are not passed as arguments.

3.3 Code validation

3.3.1 Dynamic & re-meshing mesh

This study aims to determine the optimal aerodynamic parameters maximizing the efficiency of power extraction achieved by a single foil by controlling non-uniform incoming flow or non-sinusoidal heaving motion at low Reynolds number level. At first, we tried to use dynamic mesh and re-meshing for prescribing the motion of flapping foil because of the simplicity of this dynamic mesh method, but there are critical issues of re-meshing in grid around foil while using this technique due to too small grid around foil (1000 nodes on a foil). As seen in Figure 3.3, abnormal extended grid around foil decreases the accuracy of force coefficients and remains as an obstacle to get more accurate data of velocity and vorticity field. Figure 3.4 shows that it is difficult to achieve more precise date by using dynamic & re-meshing having a mesh bulge issue. We tried to change or find optimal parameters of spring constant factor, convergence tolerance, and size re-meshing interval in dynamic & re-meshing control panel to solve this issue. To impose high precision parameters in control panel needs very high computational costs. Some test cases need 10 days to complete numerical analysis. It is easier to set up dynamic & re-meshing than sliding mesh, but we decided to change a moving mesh model from dynamic & re-meshing model to sliding mesh model.

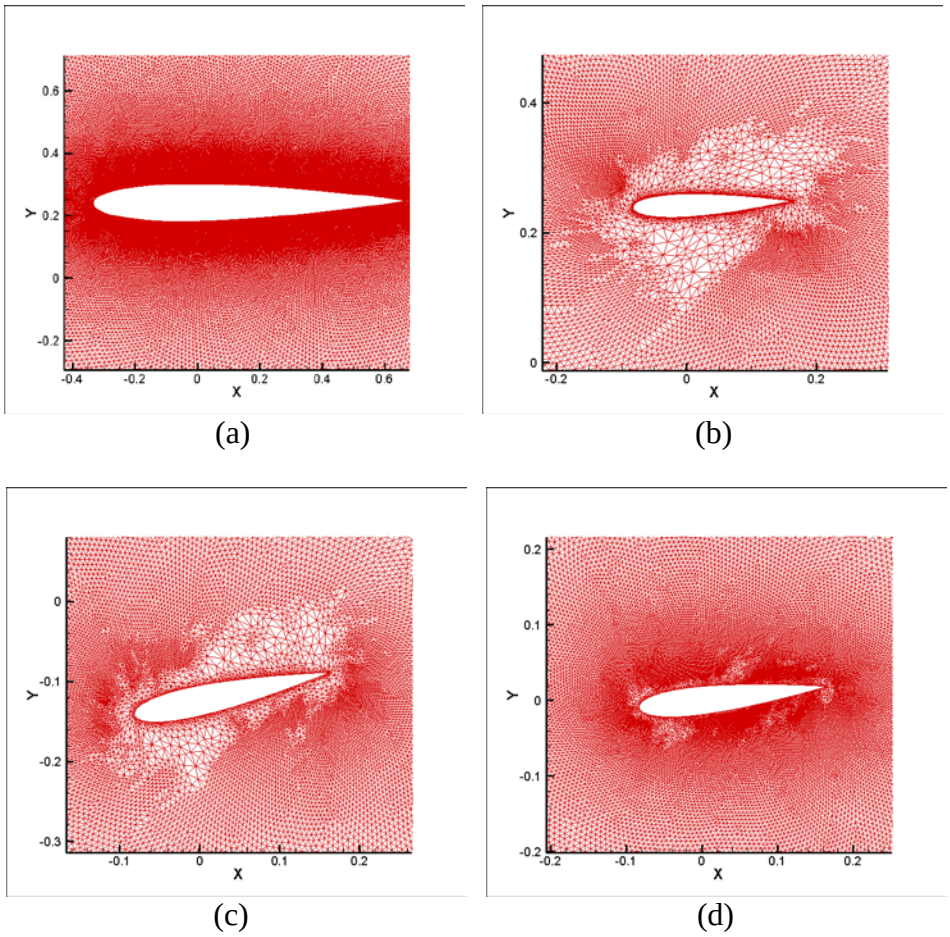

Figure 3.3: Abnormal extended grid around a foil: (a) Before starting re-meshing, (b) Spring constant factor = 1, number of iteration = 10^5, convergence tolerance = 1×10^{-9}, and size re-meshing interval = 1, (c) Spring constant factor = 0, number of iteration = 9×10^5, convergence tolerance = 1×10^{-7}, and size re-meshing interval = 1, (d) Spring constant factor = 0, number of iteration = 5×10^5, convergence tolerance = 1×10^{-7}, and size re-meshing interval = 1

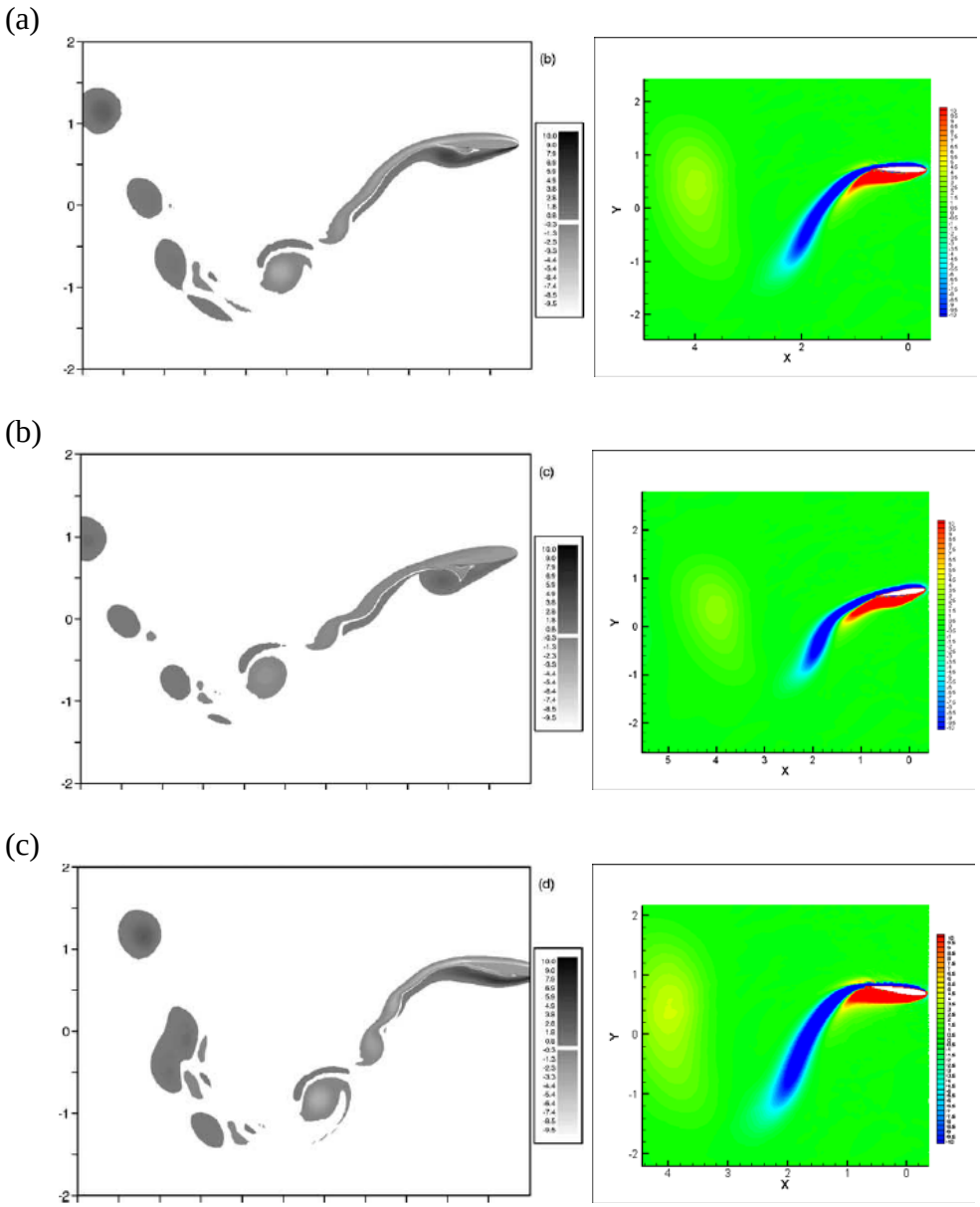

Figure 3.4: Comparison between (left column) vorticity filed by Guglielmini & Blondeaux [28] and (right column) numerical simulations by Dnamic & re-meshing mesh model about the flow field around a foil having heaving and pitching motion. The kinematic parameters are as follows: (a) St = 0.32, θ_0= 30, H_0= 0.75, ϕ= 90, (b) St = 0.32, θ_0= 30, H_0= 0.75, ϕ = 75, (c) St = 0.32, θ_0= 30, H_0= 0.75, ϕ = 105◦

3.3.2 Sliding mesh

After meeting the critical issue of dynamic and re-meshing technique, we turned to develop sliding mesh technique. We developed 2D sliding mesh models by using FLUENT 12.1 with sub-routine written in C++ to achieve accurate numerical solutions rapidly. This mesh technique is faster and results in more accurate data than dynamic and re-meshing technique. We used two different subroutines written in C++ to describe heaving and pitching motion. In addition, moving mesh motion is necessary only for the pitching motion of the foil. We divided the calculation domain into two zones bounded by a circular non-conformal sliding interface. This interface is located at four chords around the airfoil, and the grid inside interface is pitching in rigid-body motion with the airfoil. The grid outside the interface is fixed. As shown in Figure 3.5, the foil is located in the center of a very large calculation domain. The outer boundary of a computational domain is located at approximately 28 chord lengths from the foil and the non-conformal interface is located at approximately 4 chord lengths from the foil. Constant and uniform velocity is imposed at the inlet boundary while constant out flow is imposed at the outlet boundary. Sufficient near-body resolution is used to capture accurately the vorticity fields.

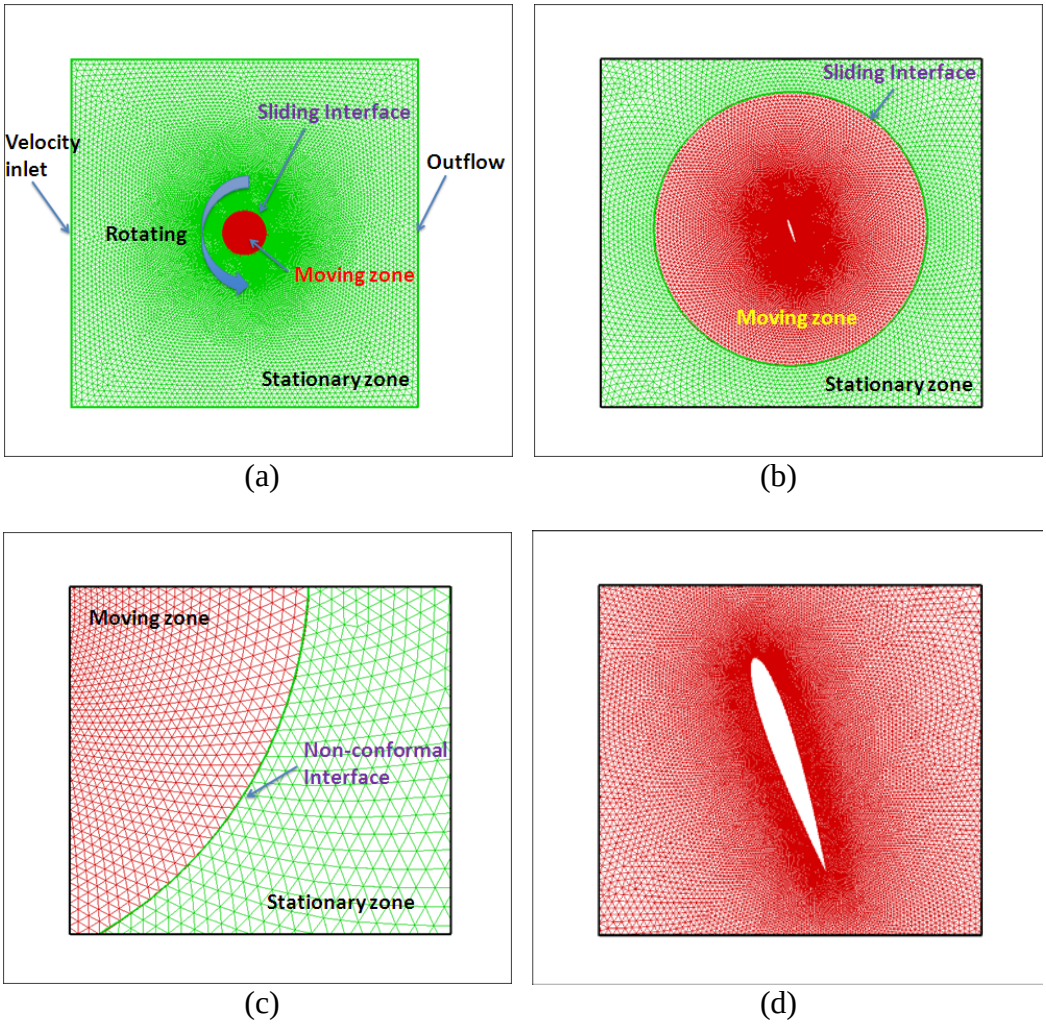

Figure 3.5: (a) The computational domain of sliding mesh, (b) Close-up view of the rotating sub-domain, (c) Close-up view of the sliding interface, (c) Close-up view of computational mesh near the foil

This method offers the significant advantage of allowing usage of second-order time integration scheme which is better than first-order when solving in a fixed inertial reference frame such as dynamic and re-meshing technique for getting higher accuracy of numerical analysis. To validate the accuracy of sliding mesh, we compare vorticity fields to data obtained from Kinsey & Dumas [14] and two types of our computations.

Figure 3.6 shows the vorticity fields of each case at t/T = 0.5. As you can see, the vorticity filed of sliding mesh technique is more similar than that of dynamic and re-mesh technique to the reference data of Kinsey & Dumas [14].

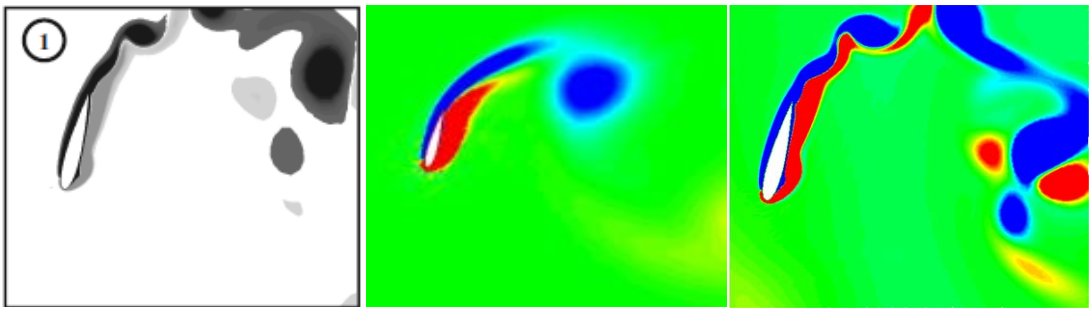

(a) (b) (c)

Figure 3.6: (a) Vorticity filed from Kinsey & Dumas, (b) Current data by dynamic and re-meshing model, (c) Current data by sliding mesh model. The kinematic parameters are as follows: f^* = 0.14, θ_0= 76.33, H_0= 1 at t/T = 0.5

We could corroborate the validity and accuracy of this Navier-Stokes solver in FLUENT through comparisons with other numerical results in terms of a flapping foil system. Energy extraction efficiency and fluid force generation are considered as main sensitive parameters for code validation. Our numerical results show that there is no transient effect on fluid forces and power extraction efficiency η after two cycles. To compute power extraction efficiency and forces and momentums of a flapping foil, we extract FLUENT data between $t = 4T$ and $5T$ ($T = 1/f$ is the cycle of oscillating). We tested the convergence of our data with respect to time refinements and space refinements. Table 3.1 lists descriptions of different time step scale and the number of grid in whole computational domain and convergence test with respect to time and mesh density.

Table 3.1: (a) Table of the number of grids, (b) Table of the time step, (c) Convergence of energy extraction efficiencies η with respect to the number of mesh grids and the time step. The kinematic parameters are as follows: f^* = 0.14, θ_0= 76.33, H_0= 1 at Re=1100.

(a)

Type	Description
Low mesh density	82,000 cells (516 nodes on a foil)
Medium mesh density	119,000 cells (516 nodes on a foil)
Fine mesh density	186,000 cells (1030 nodes on a foil)

(b)

Type	Description
Low time step	0.002 (500 iterations per 1 cycle)
Medium time step 1	0.001 (1000 iterations per 1 cycle)
Medium time step 2	0.0005 (2000 iterations per 1 cycle)
Fine time step	0.00025 (4000 iterations per 1 cycle)

(c)

	Low mesh	Medium mesh	Fine mesh
TS 002	33.7394	33.6648	32.9958
TS 001	33.0792	33.1016	33.3671
TS 0005	31.1939	31.5662	32.2273
TS 00025	29.3635	30.8259	30.1378
Average	31.8440	32.2896	32.1820

Table 3.2: (a) Table of the number of grids, (b) Table of the time step, (c) Convergence of energy extraction efficiencies η with respect to the number of mesh grids and the time step. The kinematic parameters are as follows: f^* = 0.14, θ_0= 76.33, H_0= 1 at t/T = 0.5

	Case 1	Case 2	Case 3
Kinsey & Dumas	33.7	28.5	20.8
Current method	32.2	27.6	21.2

As shown in Table 3.1 (c), we can see that the energy efficiency converged at fine mesh and time step 0.0005. The average efficiency η is obtained as 32.182, which is almost identical to the result of fine mesh and time step 0.0005 (32.227). This mesh

model is selected as a standard model for numerical studying of a flapping foil. We have also compared our energy extraction efficiency η with the results by Kinsey & Dumas [14] using FLUENT at a Reynolds number of 1100. We selected 3 cases from the results by Kinsey & Dumas [14] and tested out numerical model. It is seen that our results are generally no discrepancies in the results and consistent with those in Kinsey & Dumas [14] in table 3.2.

3.3.3 Flow solver and algorithm

High resolution two-dimensional unsteady computations are performed in this study at Reynolds numbers at 200 by using the commercial finite volume method code FLUENT 12.1 [11]. A second-order upwind spatial discretization is used, and the motion of the flapping foil is introduced by adjusting a source term in the Navier Stoked equations for the heaving motion and rotation of a circular inner zone around the foil for the pitching motion. Sliding mesh model allows second-order accurate time stepping. A pointwise Gauss–Seidel linear equation solver is used to solve the discretized equations. The velocity-pressure coupling is used on a semi implicit method for pressure-linked equations (SIMPLE) segregated algorithm.

Chapter 4

ENERGY HARVESTING PERFORMANCE IN UNIFORM FLOW

In the course of this work, numerical simulations are performed with Eulerian approach using dynamics mesh technique as a tool for vortex analysis of a flapping foil. We use GAMBIT 2.3 [10] to make geometry and to form moving grid and boundary conditions. Commercial code FLUENT 12.1[11] are used for investigate flow physics and wake around moving foil. Accuracy of this numerical simulation is validated through a rigorous validation includes spatial and temporal convergence tests as well as comparisons with previous work. A mapping of energy extraction efficiency is presented for a given single foil geometry (NACA0012), a fixed Reynolds number (Re=200), a fixed heaving amplitude (h=1), a fixed pitching amplitude ($\alpha_0 = 75$ deg), and a fixed pitching axis location ($\frac{x_p}{c} = 1/3$). Note that the dimensionless frequency is defined as $f^* = fc/U_\infty$.

4.1 Energy harvesting efficiency

For comparison of the linear shear inlet flow and the non-sinusoidal heaving motion with conventional sinusoidal motion, we simulated cases of a single foil with sinusoidal heaving motion. To concentrate the effect of our interesting parameters, all parameters were initially kept fixed, except for non-dimensional frequency. The flapping

parameters were chosen with reference to Kinsey & Dumas [14] and selected optimal parameters for getting higher power extraction efficiency. Kinsey & Dumas [14] simulated cases of a single NACA0015 foil pitching about 1/3 chord at *Re* = 1000, H_0/c = 1, $\phi = 90$ deg. Their results showed that cases in the range of non-dimensional frequency *f** = 0.12 ~ 0.16 and pitching amplitude θ_0= 70 deg ~ 80deg have high energy extraction efficiencies. In particular, the energy extraction efficiency of case of *f** =0.15 and θ_0= 75 deg at *Re*=1100 has up to 34%. This efficiency is comparable with high performance convectional rotor blade turbines. To get higher power extraction efficiency, we adopted optimal flapping parameters from results of Kinsey & Dumas [14]. This group of fixed parameters constitutes our basic configuration: NACA 0012 airfoil, Re =200, H_0/c =1, $\frac{x_p}{c} = 1/3$, and θ_0 = 75 deg. The energy harvesting efficiency as functions of the non-dimensional frequency f^* is provided in Figure 4.1. First, we find that the highest energy harvesting efficiency is obtained at non-dimensional frequencies in the range of *f** = 0.12 ~ 0.18 and efficiencies of these cases is higher than 20%. Especially, case of *f** = 0.15 show the optimal energy harvesting efficiency ($\eta =$ 25.6%). This characteristics is in agreement with results by Kinsey & Dumas [14]

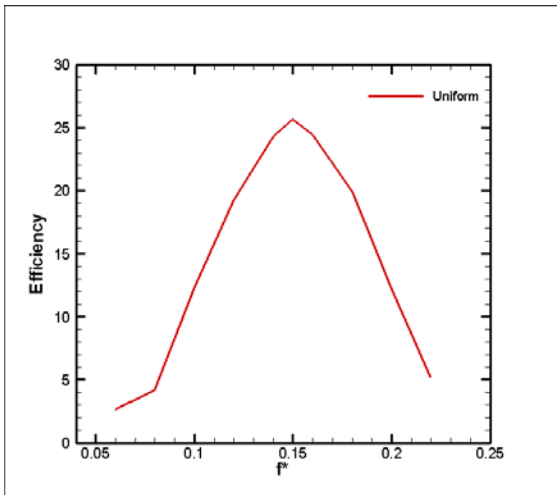

Figure 4.1: Energy harvesting efficiency as function of non-dimensional frequency. The kinematic parameters are as follows: θ_0= 75 deg, H_0/c= 1 at RE = 200

Chapter 5

ENERGY HARVESTING PERFORMANCE IN LINEAR SHEAR FLOW

5.1 Power efficiency and energy harvesting efficiency

The flapping foil system mainly is installed in shallow water sites such as river or sea base. Actually, the river velocity profile is not uniform flow due to no-slip condition of base. To simplify river velocity profile, we made linear shear profiles as inlet velocity condition for examining the effect of non uniform inlet profile. We simulated cases for mapping energy harvesting efficiency as a function of the oscillation frequency at low Reynolds number with non-uniform incoming flow. In cases of non-uniform incoming flow, we used three kinds of linear shear inlet flow that have different shear rate. At the inlet, a linear velocity profile ($u = 1 + Ky, v = w = 0$) is assumed, where K is a non-dimensional shear parameter. At the outlet boundary, the outflow condition specifies natural boundary conditions. No-slip conditions are prescribed on the body surface. Figure 5.1 shows three kinds of linear shear inlet flow that we used. The power coefficient C_{op} and energy harvesting efficiency η are two crucial parameters for the performance of energy harvesting device. We examine the effect of varying linear shear

inlet profile through the parameter *K*. Three *K* of 1.0, 2.0 and 3.0 are studied with one heaving amplitude h_0/c = 1.0 and one pitching amplitude θ_0= 75 deg. It should be noted that if the K value is zero, this condition results in the symmetry condition (uniform flow). Maximum pitching amplitude θ_0 is varied for various non-dimensional frequency *f** from 0.06 to 0.22.

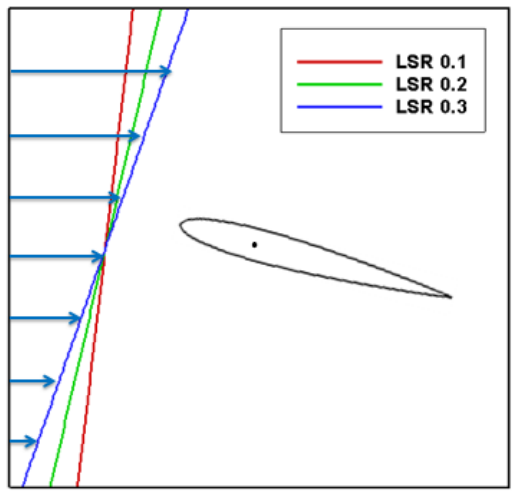

Figure 5.1: Three kinds of linear shear inlet flow that have different shear rate

The variation of time-mean output power coefficient C_{op} and energy harvesting efficiency η with non-dimensional frequency *f** for different *K* varying from 1.0 to 3.0 is shown in Figure 5.2 (a) and (b) at θ_0=75 deg and h_0/c = 1.0. Generally, curves of all cases for C_{op} and energy harvesting efficiency η versus non-dimensional frequency have some similar features. For examples, the power coefficient initially increases with non-dimensional frequency until a critical point of non-dimensional frequency, and afterward it decays with the further increasing non-dimensional frequency. Clearly seen from Figure 5.2 (a) to (b), some special features of plots are revealed for different *K* compared to a uniform inlet flow case. Output power efficiencies and energy harvesting efficiencies

slightly increase within a certain range of non-dimensional frequency by imposing linear shear inlet flow with varying *K*. In uniform flow, we find the highest power extraction efficiency achieved up to nearly 26% at non-dimensional frequency of f^*=0.15. In the range of from f^*=0.12 to f^*=0.16, efficiencies is higher than 20% for a single flapping foil. Among three cases of linear shear inlet examined, results obtained by *K*= 0.1 and 0.2 cover a certain range of non-dimensional frequency span with high energy harvesting efficiency. In fact, efficiencies of cases of *K*=0.2 have higher than other *K* value cases and that of cases of *K*=0.2 and *K*=0.1 from f^*=0.06 to f^*=0.14 have slightly higher than cases of uniform flow. The efficiency of case of f^*=0.14 in *K*=0.2 achieved up to 26% and it is the highest power extraction value in linear shear cases. All of linear shear cases from f^*=0.15 to f^*=0.22 have lower power extraction efficiency than cases of uniform flow except case of f^*=0.20 and f^*=0.22 in *K*=0.1. In the range of f^*=0.06 to f^*=0.14, cases of *K*=0.2 have higher efficiencies than other linear shear cases, but cases of K=0.1 in the range of f^*=0.15 to f^*=0.22 have higher efficiencies than other linear shear cases. Higher *K* values such as 0.4 or 0.5 is shown negative power extraction efficiencies in lower and higher non-dimensional frequencies.

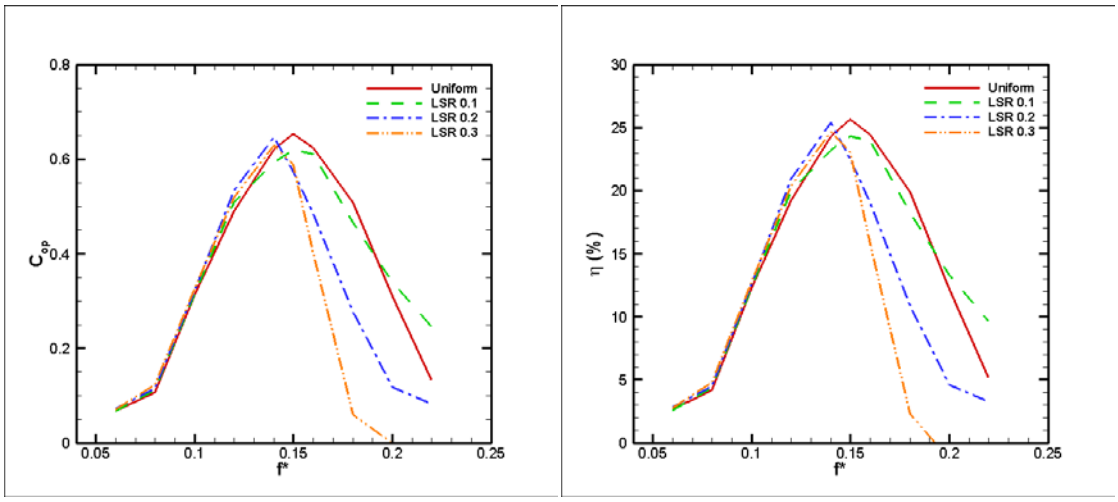

(a) (b)

Figure 5.2: (a) Comparison of time-mean output power coefficient versus non-dimensional frequencies for different *K*, (b) Comparison of time-mean energy harvesting efficiency versus non-dimensional frequencies for different *K*

Clearly, for fixed heaving amplitude and pitching amplitude, there exists an optimal *K* at which power efficiency and energy harvesting efficiency reach their maxima. The maxima of the ratio of energy harvesting efficiency in each case for varying *K* are regarded as a main criteria indicating whether the power output performance is improved. The maximum of the ratio of energy harvesting efficiency occurs at K = 0.2 and f^*=0.12 with an increment of 9 % over uniform inlet flow case. However, the smallest the ratio of energy harvesting efficiency is obtained in K = 0.3 at f^*=0.22 with a decay of -225% compared to uniform inlet flow case. Cases with K = 0.3 at f^*=0.20 and 0.22 have negative value of energy harvesting efficiency. Except these two cases, the smallest the ratio of energy harvesting efficiency occurs at K = 0.3 and f^*=0.18 with a decay of -88% compared to uniform inlet flow case. The results show that non-dimensional frequency f^* of 0.14 is the critical non-dimensional frequency. Cases of lower frequencies than 0.14 in all *K* are have increment over uniform inlet flow case, but Cases of higher frequencies

than 0.14 have decay compared to uniform inlet flow case.

5.2 Mechanism of energy harvesting capacity enhancement

For investigating the mechanism of the effect of *K* on the energy harvesting capacity, we examined the details of flow in terms of individual contributions from heaving motion and pitching motion, vorticity fields and pressure fields. Two non-dimensional frequency values of 0.14 and 0.18 are selected due to the best case and the worst case in energy harvesting efficiency among all of frequency range.

Figure 5.3 (a) - (h) show the evolution of C_L, dh/dt, C_M and $d\theta/dt$ of cases with f^* of 0.14 in one cycle for uniform flow and linear shear flow of K = 1.0, 2.0 and 3.0. Moreover, Figure 5.4 (a) - (h) show the evolution of C_L, dh/dt, C_M and $d\theta/dt$ of cases with f^* of 0.18 in one cycle for uniform flow and linear shear flow of K = 1.0, 2.0 and 3.0. Cases in Figure 5.3 and Figure 5.4 show that the heaving contribution to total energy extraction considerably dominates the pitching contribution because small moment coefficient makes small overall contribution. It is seen that our results are generally no discrepancies in the results and consistent with those in Kinsey & Dumas [14]. As seen in Equation (2.12), if C_L and dh/dt (or C_M and $d\theta/dt$) have the same sign, that will be positive contribution to the total energy extraction while those have opposite sign, resulting in a negative contribution to the total energy extraction.

Cases of f^* of 0.14 show that C_L and dh/dt have the same sign over almost all of the cycle and have very similar plots. It is seen that the variation of these plots of cases are consistent with that of power efficiency and energy harvesting efficiency. That means

there are no significant variations from these plots. On the other hand, Cases of f^* of 0.18 show that C_L and *dh/dt* have the different sign over almost all of the cycle except middle interval. As seen, with the increase of *K* in higher non-dimensional frequency, the magnitude of C_L of negative sign part increase or overall magnitude of C_L decrease and thus have less negative effect on heaving contribution of total energy harvesting capacity. This is shown by Figure 4.5 in which one can easily find the variation of the magnitude of C_L plots.

Consequently, C_L may have positive effect on energy harvesting with lower non-dimensional frequencies ($f^* < 0.15$). However, C_L has negative effect on energy harvesting with higher non-dimensional frequencies ($f^* \geq 0.15$). These influences become much stronger with larger *K*, because the magnitudes of C_L interval that has different sign with *dh/dt* increase dramatically with the increase of *K* as well as the overall magnitude of C_L decrease in all of the cycle.

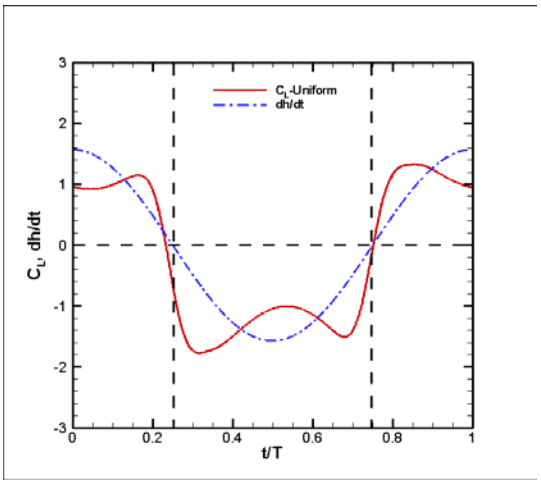

(a) C_L and *dh/dt*

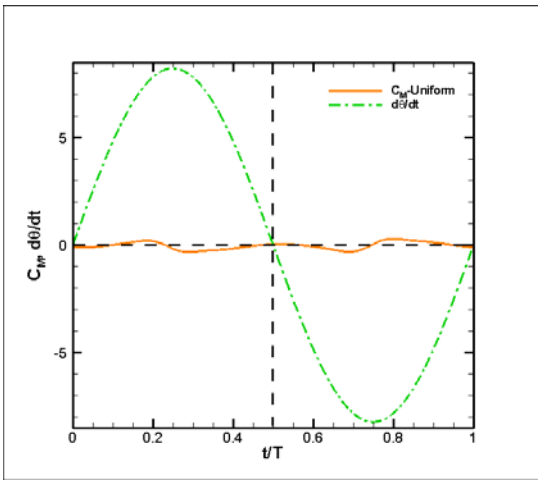

(b) C_M and *dθ/dt*

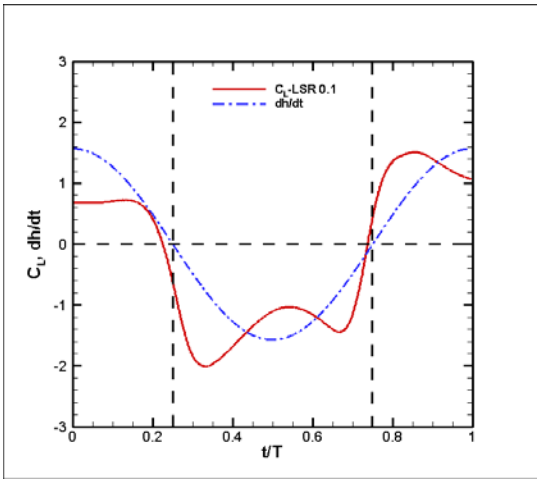

(c) C_L and *dh/dt*

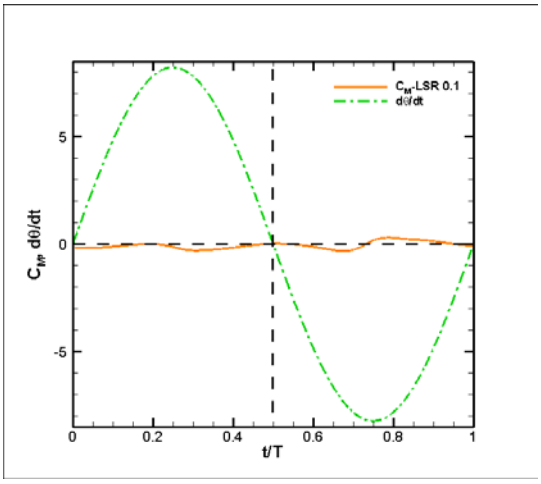

(d) C_M and *dθ/dt*

Figure 5.3: Plots of lift coefficient (C_L), heaving velocity (*dh/dt*), momentum coefficient (C_M) and pitching velocity (*dθ/dt*) in one cycle. (a - b) $f^* = 0.14$ in uniform flow, (c - d) $f^* = 0.14$ in linear shear flow ($K = 0.1$), (e - f) $f^* = 0.14$ in linear shear flow ($K = 0.2$), (g - h) $f^* = 0.14$ in linear shear flow ($K = 0.3$)

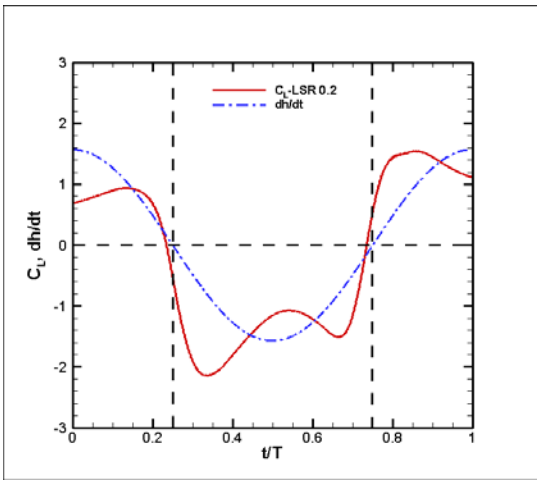

(e) C_L and *dh/dt*

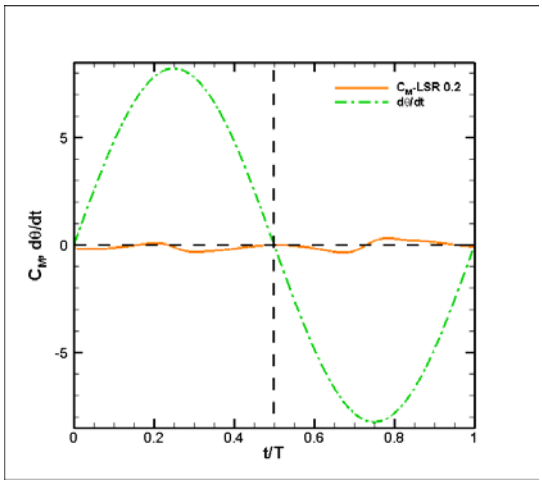

(f) C_M and *dθ/dt*

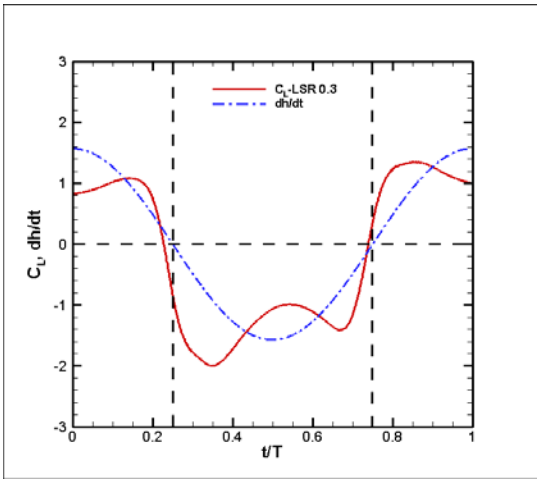

(g) C_L and *dh/dt*

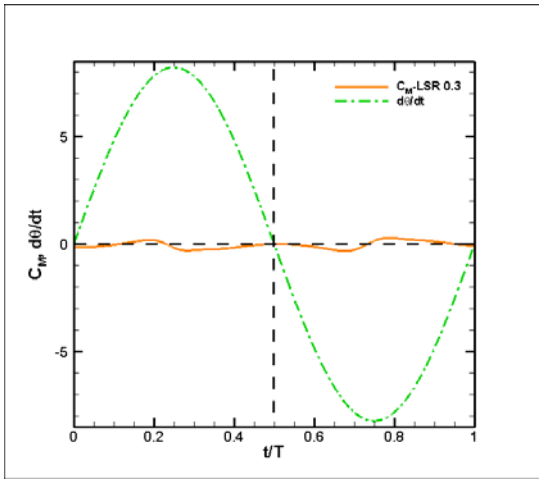

(h) C_M and *dθ/dt*

Figure 5.3(continue): Plots of lift coefficient (C_L), heaving velocity (*dh/dt*), momentum coefficient (C_M) and pitching velocity (*dθ/dt*) in one cycle. (a - b) $f^* = 0.14$ in uniform flow, (c - d) $f^* = 0.14$ in linear shear flow ($K = 0.1$), (e - f) $f^* = 0.14$ in linear shear flow ($K = 0.2$), (g - h) $f^* = 0.14$ in linear shear flow ($K = 0.3$)

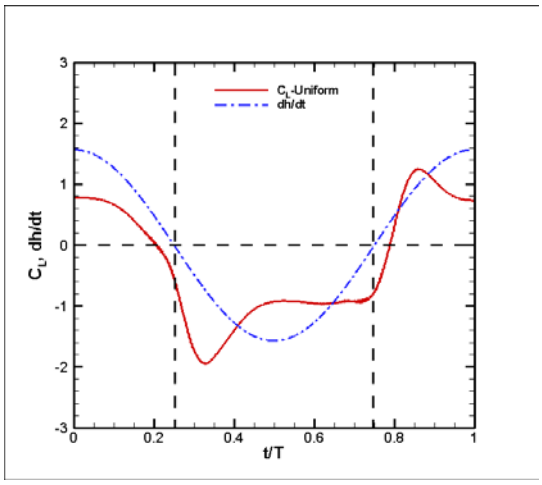

(a) C_L and *dh/dt*

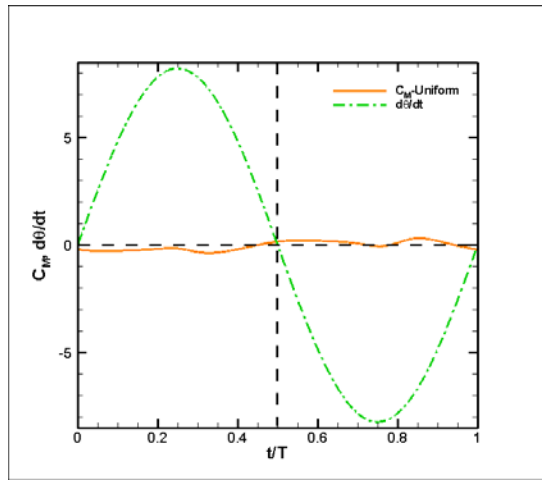

(b) C_M and *dθ/dt*

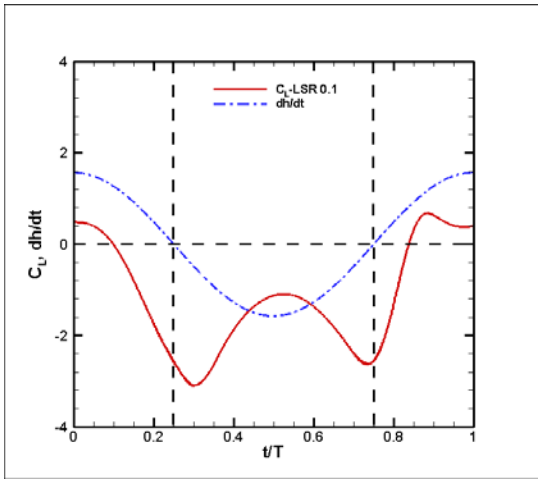

(c) C_L and *dh/dt*

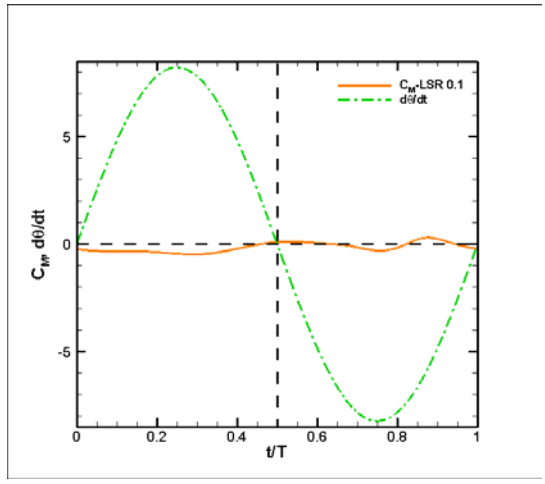

(d) C_M and *dθ/dt*

Figure 5.4: Plots of lift coefficient (C_L), heaving velocity (*dh/dt*), momentum coefficient (C_M) and pitching velocity (*dθ/dt*) in one cycle. (a - b) $f^* = 0.18$ in uniform flow, (c - d) $f^* = 0.18$ in linear shear flow ($K = 0.1$), (e - f) $f^* = 0.18$ in linear shear flow ($K = 0.2$), (g - h) $f^* = 0.18$ in linear shear flow ($K = 0.3$)

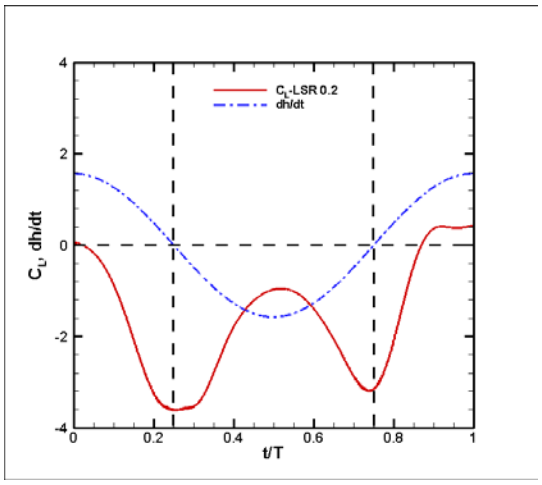

(e) C_L and *dh/dt*

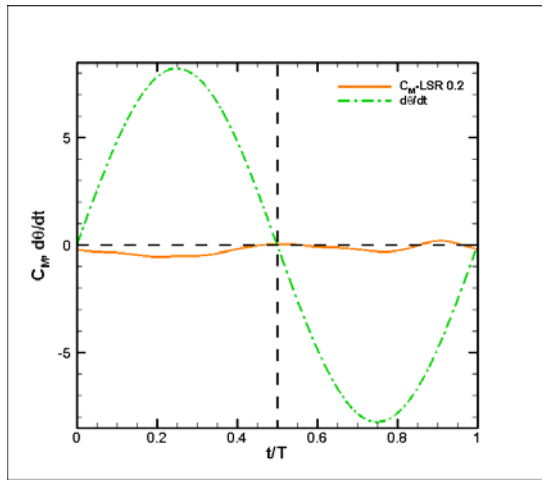

(f) C_M and *dθ/dt*

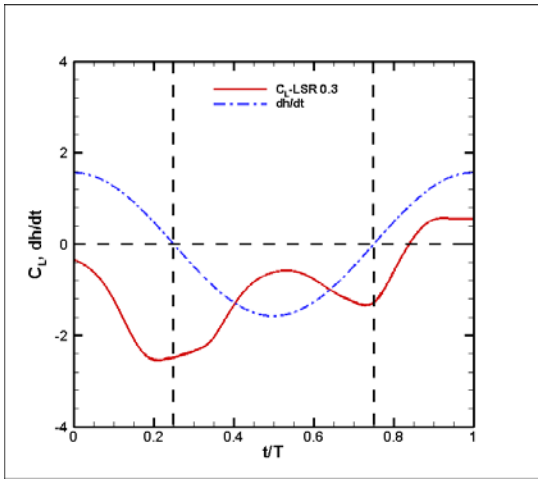

(g) C_L and *dh/dt*

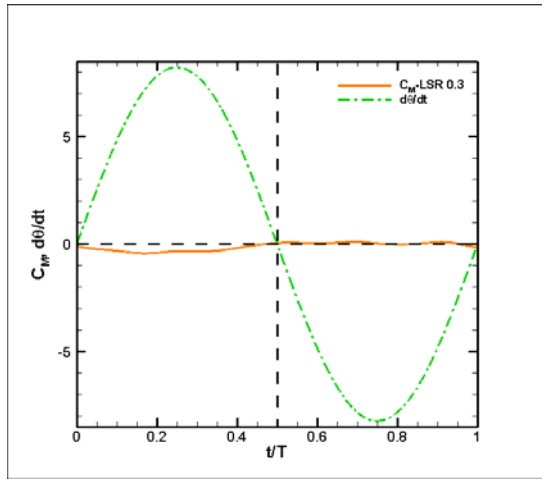

(h) C_M and *dθ/dt*

Figure 5.4(continue): Plots of lift coefficient (C_L), heaving velocity (*dh/dt*), momentum coefficient (C_M) and pitching velocity (*dθ/dt*) in one cycle. (a - b) $f^* = 0.18$ in uniform flow, (c - d) $f^* = 0.18$ in linear shear flow ($K = 0.1$), (e - f) $f^* = 0.18$ in linear shear flow ($K = 0.2$), (g - h) $f^* = 0.18$ in linear shear flow ($K = 0.3$)

Taking a close up examination of near-body flow fields is very useful for investigating on the mechanism of energy harvesting. We took a close up observation the vorticity field around the foil of above cases in Figure 5.5~5.8. Case of f^*=0.14 in uniform flow and case of f^*=0.14 in linear shear flow (K = 0.2) have nearly same vorticity structure and evolution.

In Figure 5.5 and 5.6, a leading edge vortex (LEV) formed near the leading edge and grows and moves to the trailing edge. Afterward, a leading edge vortex interacts with the rest part of the foil before shedding into the wake. When the LEV evolves along with the upper surface of a foil, low pressure on the foil surface is created. This low surface pressure distribution generates at the upper surface of the foil close to the trailing edge as seen from Figure 5.9 and 5.10. The surface pressure distribution will play a major role in generating aerodynamic forces such as lift coefficient which is effectively related to the energy harvesting efficiency. This low pressure makes a counterclockwise pitching moment and the motion of the flapping foil is counterclockwise rotation. In addition, from t/T = 0.25 to t/T = 0.5, the pressure distribution of lower surface of the foil is smaller than that of upper surface of the foil when a secondary vortex on upper surface of the foil is induced by the first LEV. This means that negative effective angle of attack (AOA) results in negative downward lift. These processes indicated that the direction aerodynamic forces by induced pressure distribution are identical to the direction of prescribed flapping motion. Synchronization between the movement of the foil and the evolution of the near-body vorticity field contributes to make a positive product $C_L \cdot dh/dt$ in this interval. Obviously, a positive product $C_L \cdot dh/dt$ discussed above is enable to extract energy from the flow field. The magnitude of LEV and pressure distribution around the foil almost unchanged even if K value increases in lower non-dimensional frequency (< critical frequency f^* = 0.14)

As shown in Figure 5.7 and 5.8, a different dynamic behavior is observed in higher non-dimensional frequency. Interactions between LEV and the foil are similar to

aforementioned manner. However, the shedding of LEV is faster than the cases of lower non-dimensional frequency, and low pressure induced by LEV on the upper foil surface diminished faster than previous cases. This mechanism is bad synchronization between the movement of the foil and the evolution of the near-body vorticity field. Cleary, this interaction contributes to form a negative product $C_L \cdot dh/dt$ in this interval. For such a reason, there are no advantages to get energy harvesting from this interaction. Moreover, the LEV becomes weaker with K increasing in higher non-dimensional frequency (> critical frequency $f^* = 0.14$), and it seems that the mechanism of LEV discussed above does not have crucial impact on the pressure distributions. As we can see Figure 5.11 and 5.12, the magnitude of pressure distribution is smaller than lower non-dimensional frequency cases. Staying LEV on the foil surface can improve the lift force and would be advantage to energy harvesting. Synchronization between the foil movements and the evolution of vorticity field is important thing to power generation.

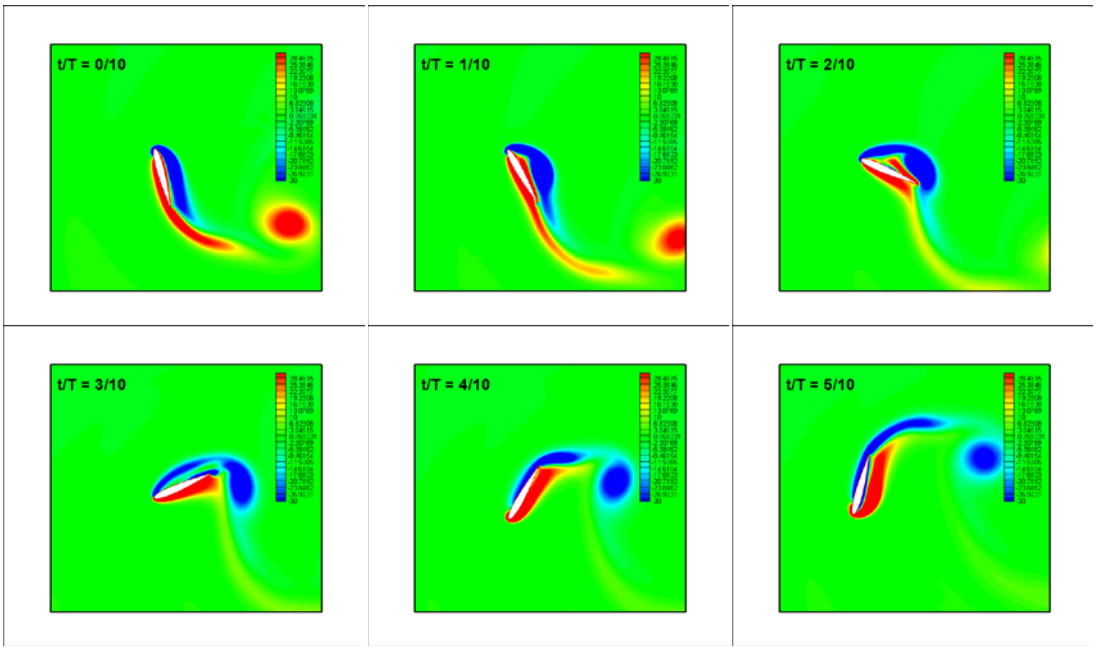

Figure 5.5: Vorticity fields at f^* of 0.14 in uniform inlet flow

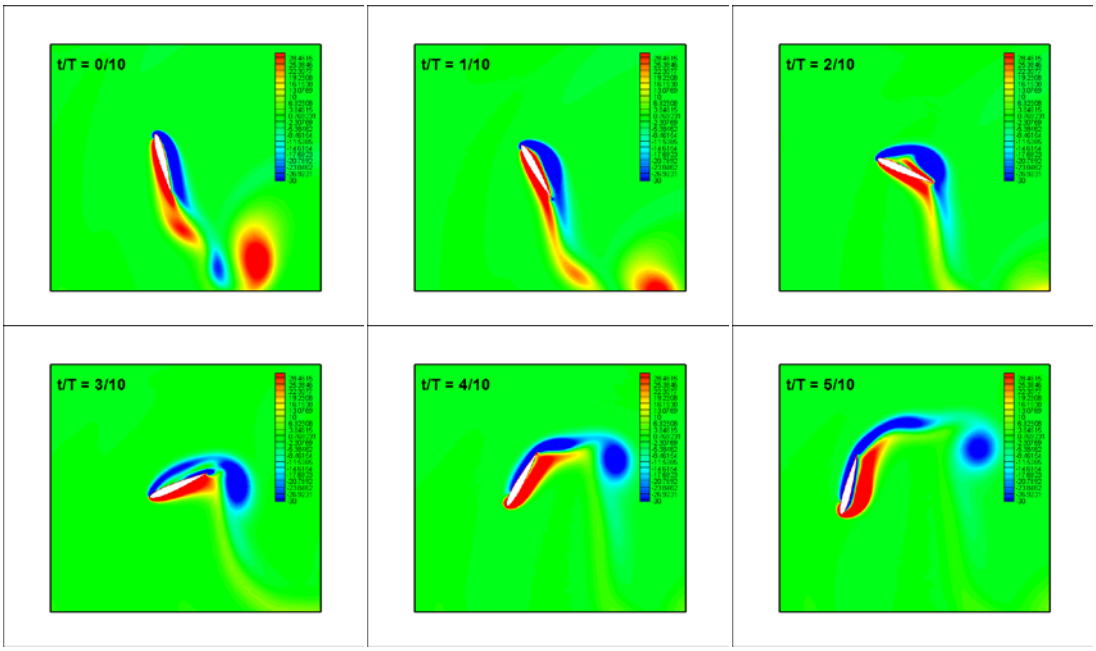

Figure 5.6: Vorticity fields at f^* of 0.14 in linear shear flow (K = 0.2)

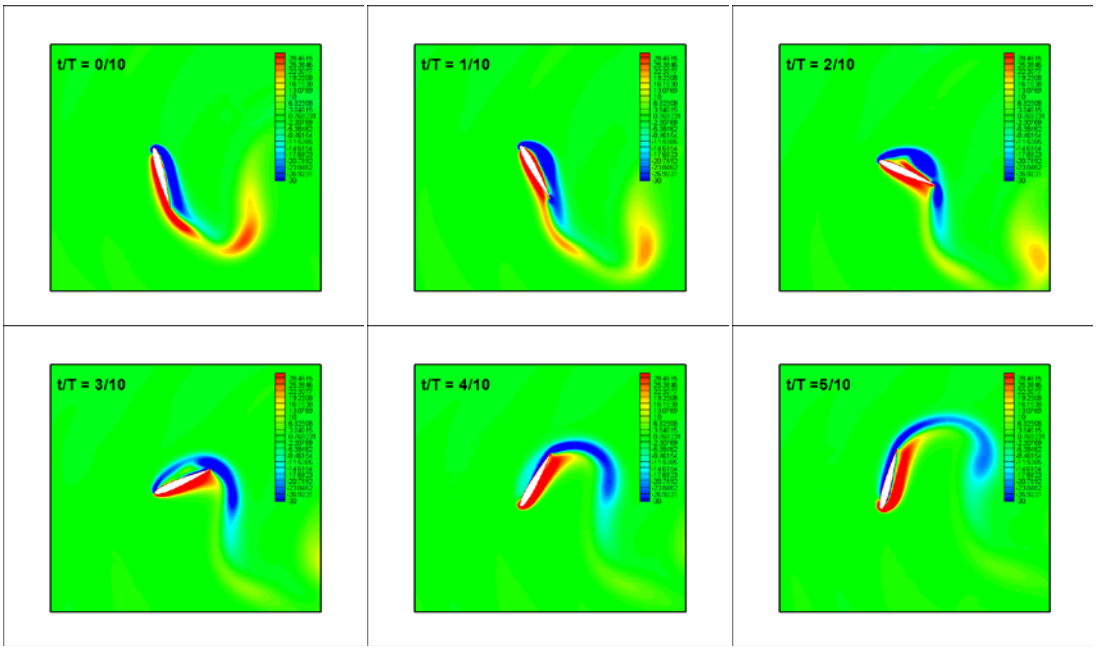

Figure 5.7: Vorticity fields at *f** of 0.18 in uniform inlet flow

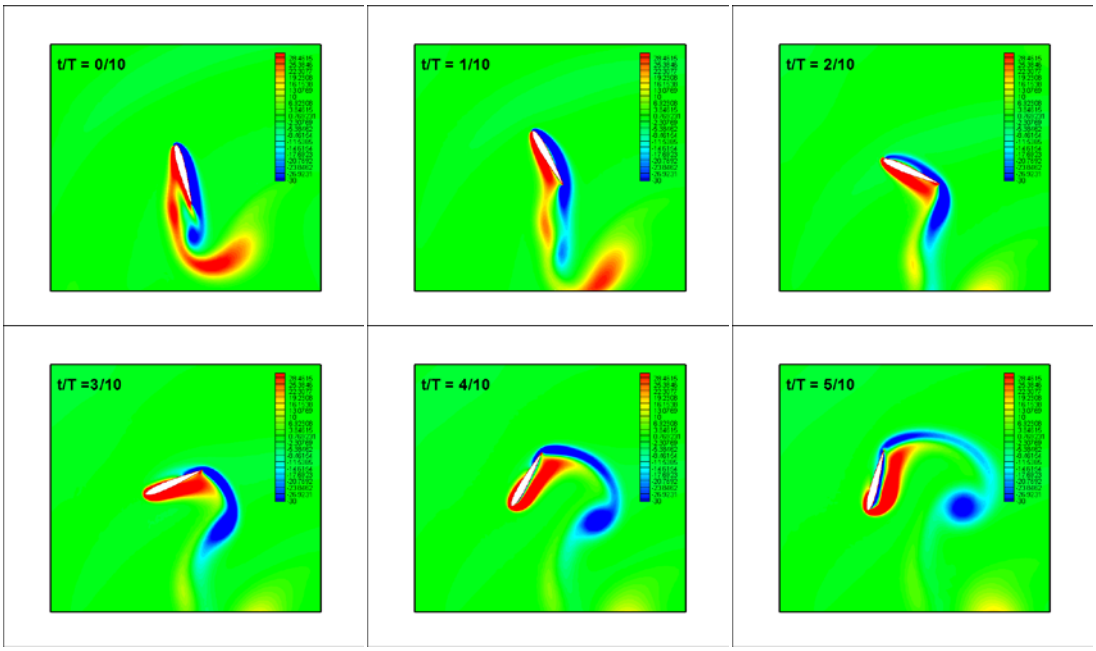

Figure 5.8: Vorticity fields at *f** of 0.18 in linear shear flow (K = 0.2)

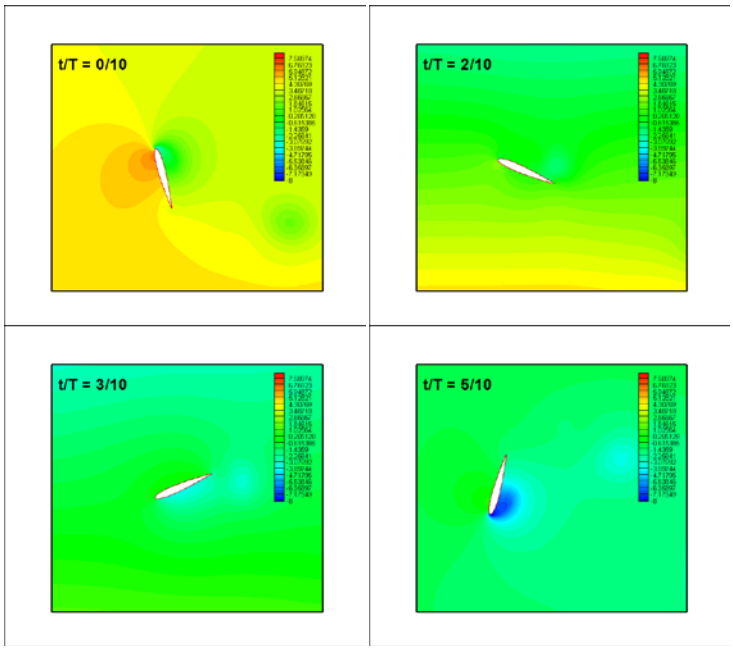

Figure 5.9: Pressure fields at *f** of 0.14 in uniform inlet flow

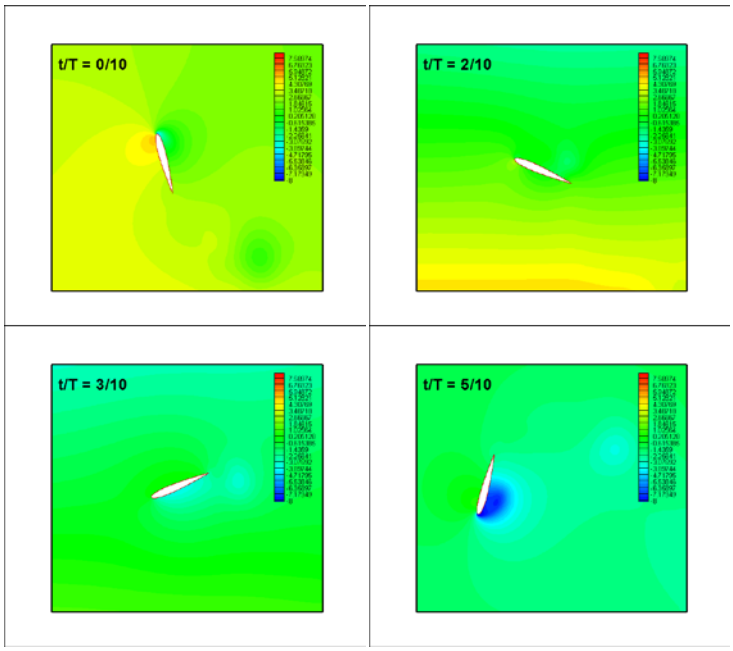

Figure 5.10: Pressure fields at *f** of 0.14 in linear shear flow (K = 0.2)

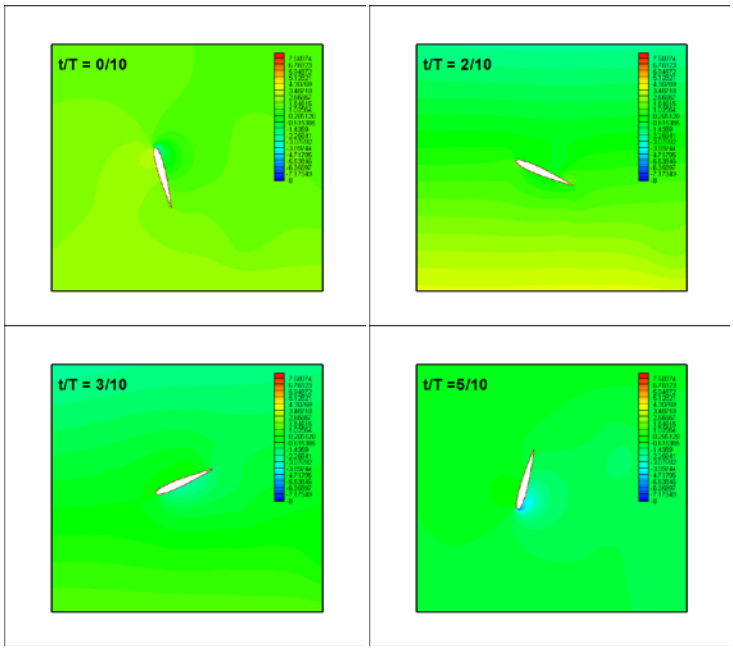

Figure 5.11: Pressure fields at *f** of 0.18 in uniform inlet flow

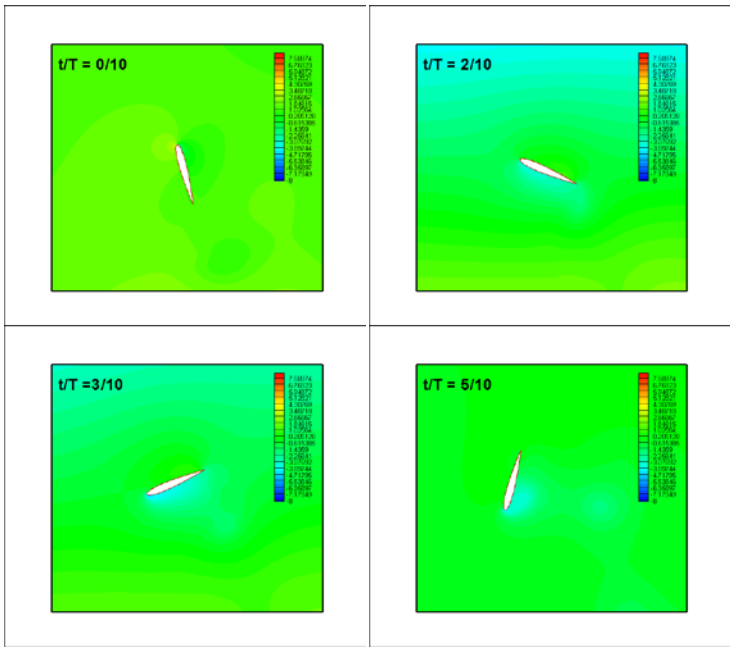

Figure 5.12: Pressure fields at *f** of 0.18 in linear shear flow (K = 0.2)

Chapter 6

ENERGY HARVESTING PERFORMANCE IN NON-SINUSOIDAL HEAVING MOTION

6.1 Power efficiency and energy harvesting efficiency

For better performance of a flapping foil for energy harvesting, researcher have started to studied non-sinusoidal motions. Non-sinusoidal motions like square wave form and triangular wave form are adopted to pitching motion and heaving motion, respectively by M. F. Platzer et al. [18, 19]. Qing Xiao et al. [20, 21] also used non-sinusoidal motion like trapezoidal wave motion for prescribing pitching motion for enhancing energy extraction performance. Non sinusoidal heaving motions used in this study are composed of two different types of waveform: trapezoidal waveform and triangular waveform. These waveforms are inspired by results of the kinematics of insect wing for energy conservation [25, 26]. We made non-sinusoidal heaving motions based on these previous insect flight studies.

The variation of time-mean output power coefficient C_{op} and energy harvesting efficiency η with non-dimensional frequency f^* for different D of trapezoidal heaving motion is shown in Figure 6.1 (a) and (b) at θ_0=75 deg and h_0/c = 1.0. Generally, curves of all cases for C_{op} and energy harvesting efficiency η versus non-dimensional

frequency have some similar features. For examples, the power coefficient initially increases with non-dimensional frequency until a critical point of non-dimensional frequency, and afterward it decays with the further increasing non-dimensional frequency.

Clearly seen from Figure 6.1 (a) to (b), some special features of plots are revealed for different *D* compared to a sinusoidal heaving motion case. In sinusoidal heaving motion case, we find the maximum power extraction efficiency achieved up to nearly 26% at non-dimensional frequency of $f^*=0.15$. In the range of from $f^*=0.12$ to $f^*=0.16$, efficiencies is higher than 20% for a single flapping foil. Output power efficiencies and energy harvesting efficiencies slightly increase within lower non-dimensional frequency by imposing H1 type of trapezoidal heaving motion. However, overall time-mean output power coefficient C_{op} and energy harvesting efficiency η by trapezoidal heaving motions is smaller than sinusoidal heaving motion except H1 case. In addition, efficiencies of trapezoidal heaving motion case are lower with decrease of *D* value.

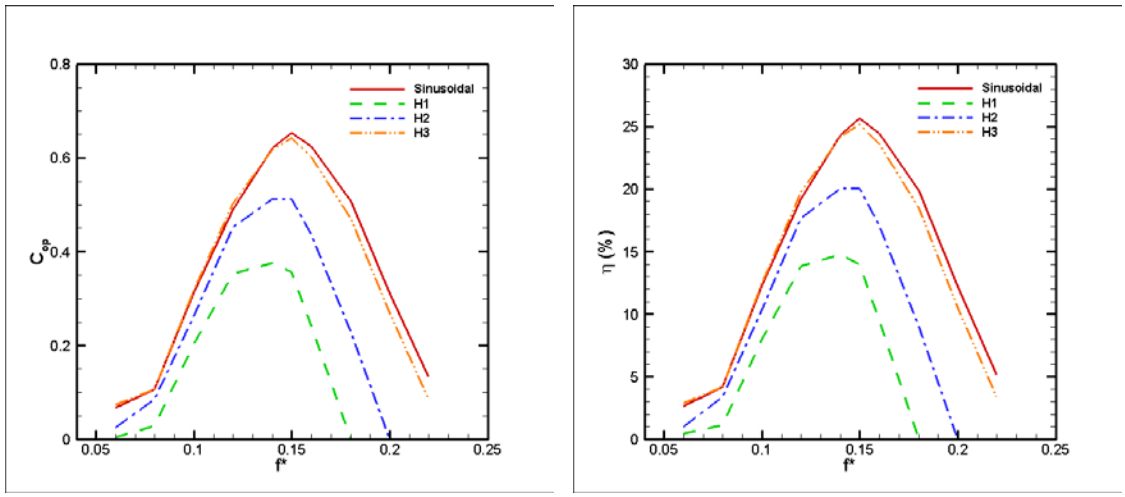

(a) (b)

Figure 6.1: (a) Comparison of time-mean output power coefficient versus non-dimensional frequencies for different *D* of trapezoidal heaving motion, (b) Comparison of time-mean energy harvesting efficiency versus non-dimensional frequencies for different *D* of trapezoidal heaving motion

The variation of time-mean output power coefficient C_{op} and energy harvesting efficiency η with non-dimensional frequency f^* for different *G* of trapezoidal heaving motion is shown in Figure 6.2 (a) and (b) at θ_0=75 deg and h_0/c = 1.0. Curves of all cases for C_{op} and energy harvesting efficiency η versus non-dimensional frequency also have some similar features. The power coefficient initially increases with non-dimensional frequency until a critical point of non-dimensional frequency, and afterward it decays with the further increasing non-dimensional frequency like trapezoidal heaving motion.

As seen from Figure 6.2 (a) to (b), some special features of plots are revealed for different *G* compared to a sinusoidal heaving motion case. It seems that overall output power efficiencies and energy harvesting efficiencies is slightly lower than sinusoidal heaving motion cases, but these efficiencies slightly increase within higher non-

dimensional frequency by imposing triangular heaving motion. Efficiencies of cases of H6 have higher than other *G* value cases relatively and that of cases of H5 and H6 from *f**=0.16 to *f**=0.22 have slightly higher than cases of sinusoidal heaving motion. The efficiency of case of *f**=0.15 in H5 and H6 achieved up to 26% and it is the highest power extraction value in triangular heaving motion cases.

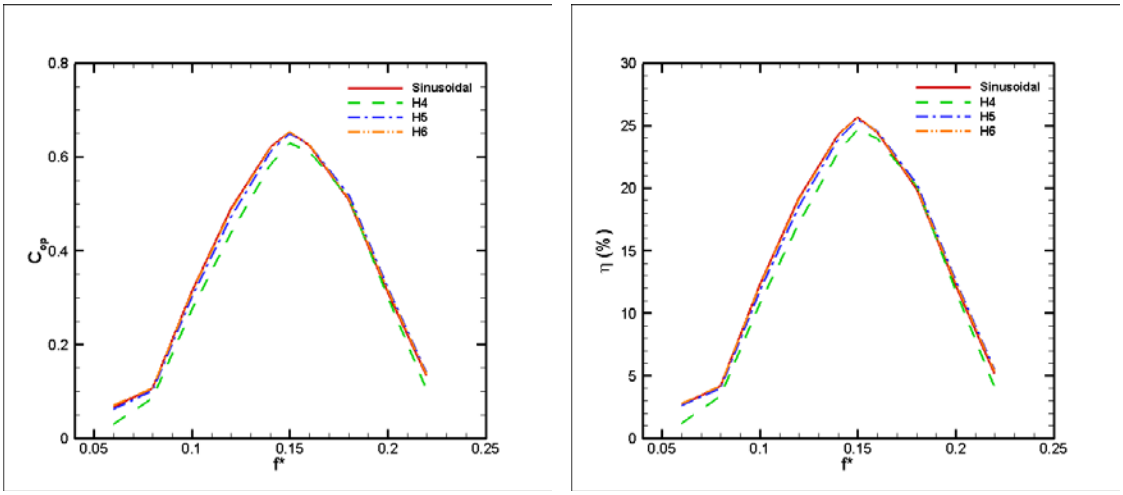

(a) (b)

Figure 6.2: (a) Comparison of time-mean output power coefficient versus non-dimensional frequencies for different *G* of triangular heaving motion, (b) Comparison of time-mean energy harvesting efficiency versus non-dimensional frequencies for different *G* of triangular heaving motion

The maxima of the ratio of energy harvesting efficiency in non-sinusoidal heaving motion for varying *D* and *G* are regarded as a main criteria indicating whether the power output performance is enhanced. The maximum of the ratio of energy harvesting efficiency occurs at H3 of *f**=0.12 and H5 of *f**=0.20 with an increment of 3% over sinusoidal heaving motion case. However, the smallest the ratio of energy harvesting efficiency is obtained in H2 at *f**=0.22 with a decay of - 254% compared to sinusoidal heaving motion case. Cases with H1 and H2 at *f**=0.20 and 0.22 have negative value of

energy harvesting efficiency. Except these cases, the smallest the ratio of energy harvesting efficiency occurs at H2 and f^*=0.18 with a decay of -55% compared to uniform inlet flow case. Generally, triangular heaving motion is much better than trapezoidal heaving motion in terms of energy harvesting efficiency.

6.2 Mechanism of energy harvesting capacity enhancement

For investigating the mechanism of the effect of D and G on the energy harvesting capacity, we examine the details of flow in terms of individual contributions from heaving motion and pitching motion, vorticity fields and pressure fields and. H1, H3, H4 and H6 with f^* of 0.15 of are selected due to the best case and the worst case in energy harvesting efficiency among all of frequency range, respectively.

Figure 6.3 (a) - (f) show the evolution of C_L, dh/dt, C_M and $d\theta/dt$ of cases with f^* of 0.15 in one cycle for sinusoidal heaving motion and trapezoidal heaving motion (H1 and H3). Moreover, Figure 6.4 (a) - (f) show the evolution of C_L, dh/dt, C_M and $d\theta/dt$ of cases with f^* of 0.15 in one cycle for sinusoidal heaving motion and triangular heaving motion (H4 and H6). Cases in Figure 6.3 and Figure 6.4 show that the heaving contribution to total energy extraction considerably dominates the pitching contribution because small moment coefficient makes small overall contribution. It is same behavior as linear shear flow cases.

Cases of trapezoidal heaving motion (H1 and H3) show that C_L and dh/dt have the same sign over almost all of the cycle and have very similar plots. However, It is noteworthy that heaving velocity dh/dt at foil stroke reversal intervals (t/T = 0.25 and

0.75) is zero. Obviously, their product at foil stroke reversal intervals has no contribution to energy harvesting. With *D* increasing, the portion of zero heaving velocity intervals enlarges and it makes lower power extraction efficiency. As seen in Figure 6.1, we can see the energy harvesting efficiency of H1 is worse than that of H3 due to this mechanism. Zero heaving velocity intervals in trapezoidal heaving motion make negative contribution to energy harvesting efficiency.

On the other hand, Cases of f^* of triangular heaving motion also show that C_L and *dh/dt* have the same sign over almost all of the cycle. Energy extraction in the triangular heaving motion cases mainly depends on the foil stoke reversal time. The foil stoke reversal time is shorter with increasing *G*. A large energy input (or negative energy) is required to initiate the foil rotation for small the stroke reversal time. As seen, with the increase of *G* in lower non-dimensional frequency, energy consumption would be needed more than other cases. In this study, the gap of *G* value is quite small, so there is no significant difference of each triangular case. It is seen that the variation of these plots of cases are consistent with that of power efficiency and energy harvesting efficiency. That means there are no significant variations from these plots.

Consequently, triangular heaving motion may have positive effect on energy harvesting with higher non-dimensional frequencies ($f^* > 0.18$). However, trapezoidal heaving motion has negative effect on energy harvesting with all of non-dimensional frequencies except H3. Zero heaving velocity and the foil stroke reversal time is mainly key point to non-sinusoidal heaving motion. These influences become much stronger with larger *D* and *G*.

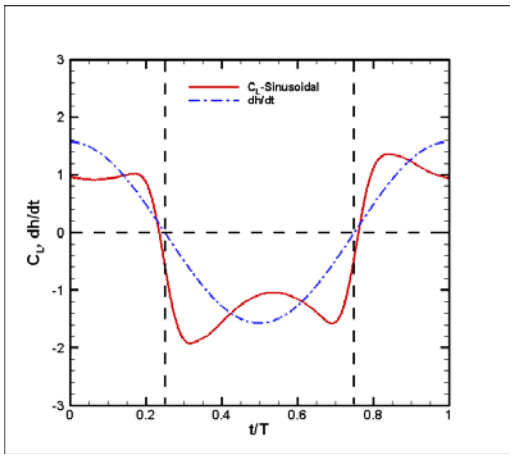

(a) C_L and *dh/dt*

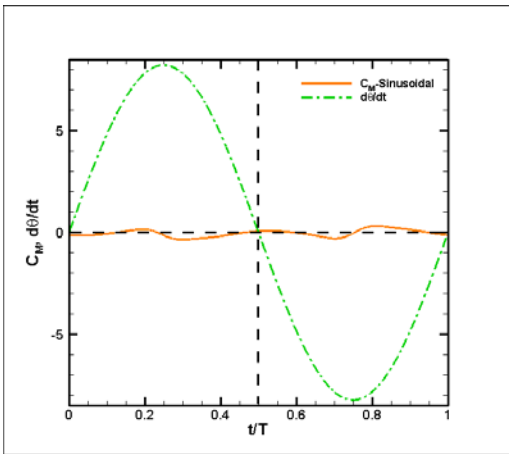

(b) C_M and *dθ/dt*

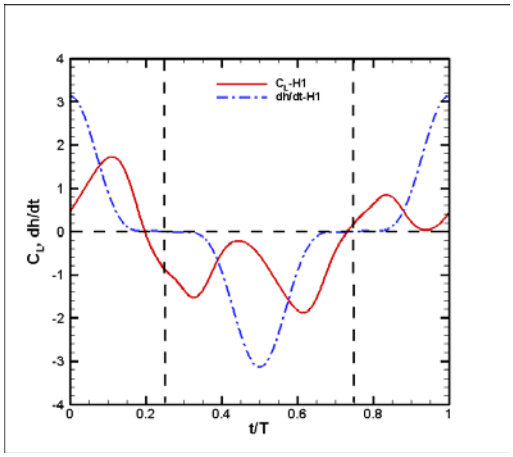

(c) C_L and *dh/dt*

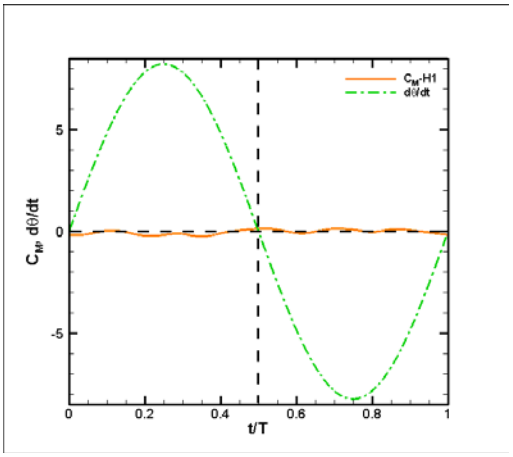

(d) C_M and *dθ/dt*

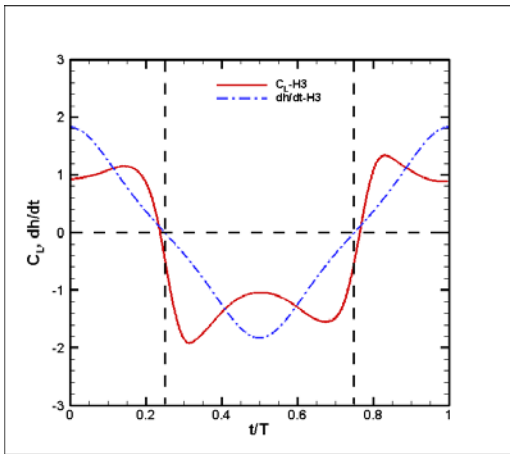

(e) C_L and *dh/dt*

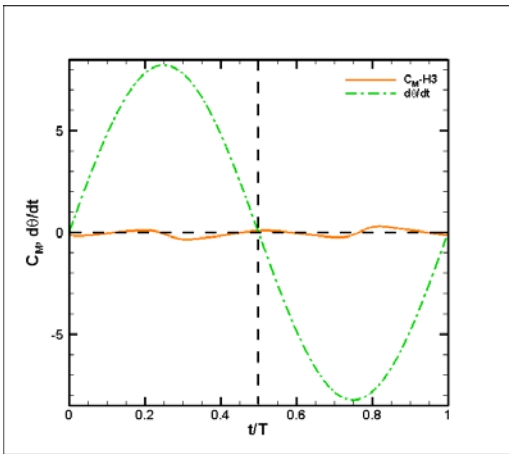

(f) C_M and *dθ/dt*

Figure 6.3: Plots of lift coefficient (C_L), heaving velocity (*dh/dt*), momentum coefficient (C_M) and pitching velocity (*dθ/dt*) in one cycle. (a - b) $f^* = 0.15$ in sinusoidal heaving motion, (c - d) $f^* = 0.15$ in H1 ($D = 1.532$), (e - f) $f^* = 0.15$ in H3 ($D = 0.711$)

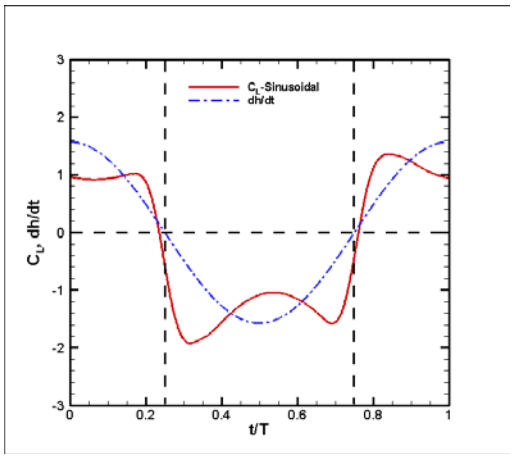

(a) C_L and *dh/dt*

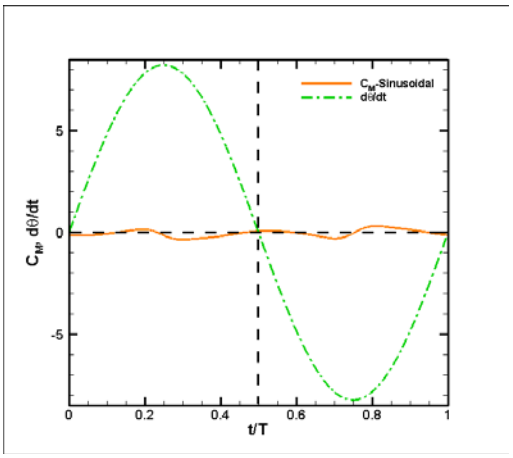

(b) C_M and *dθ/dt*

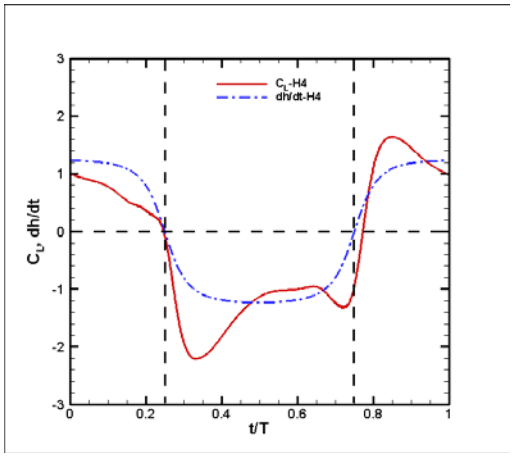

(c) C_L and *dh/dt*

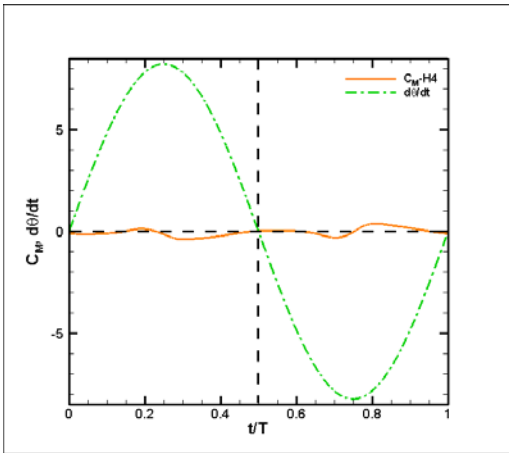

(d) C_M and *dθ/dt*

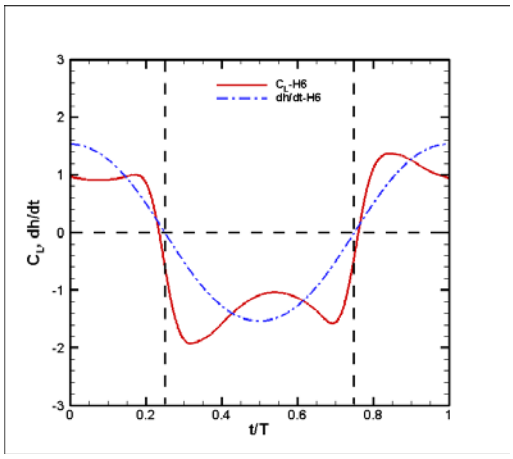

(e) C_L and *dh/dt*

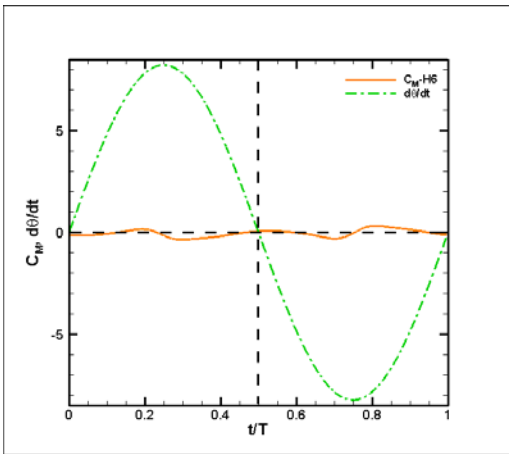

(f) C_M and *dθ/dt*

Figure 6.4: Plots of lift coefficient (C_L), heaving velocity (*dh/dt*), momentum coefficient (C_M) and pitching velocity (*dθ/dt*) in one cycle. (a - b) $f^* = 0.15$ in sinusoidal heaving motion, (c - d) $f^* = 0.15$ in H4 ($G = 0.925$), (e - f) $f^* = 0.15$ in H6 ($G = 0.354$)

We took a close up observation the vorticity field around the foil of above cases in Figure 6.5~5.9. Case of f^*=0.15 in sinusoidal heaving motion, case of f^*=0.15 in trapezoidal heaving motion (H1 and H3) and f^*=0.15 in triangular heaving motion (H4 and H6) have nearly same vorticity structure and evolution.

As seen in Figure 6.5 and 6.7, the vorticity structure of f^*=0.15 in sinusoidal heaving motion and H3 is almost same as f^*=0.14 in uniform flow. The low pressure on the foil surface is created by LEV edge as seen from Figure 6.10 and 6.12. The pitching moment by induced this low pressure and the motion of the flapping foil is counterclockwise rotation. In addition, from t/T = 0.25 to t/T = 0.5, the pressure distribution of lower surface of the foil is smaller than that of upper surface of the foil. Negative effective angle of attack (AOA) results in negative downward lift at that time. This synchronization between the foil movement and the evolution of the vorticity field contributes to make a positive product $C_L \cdot dh/dt$ in this interval. Triangular heaving motion cases (H4 and H6) also have analogous vorticity structure (Figure 6.8 and 6.9) and pressure distribution (Figure 6.13 and 6.14) Clearly, a positive product $C_L \cdot dh/dt$ discussed above can extract energy from the flow field.

As shown in Figure 6.6, Trapezoidal heaving motion H1 shows a different dynamic behavior. Interactions between LEV and the foil are similar to aforementioned manner. However, the shedding of LEV is slower than the cases of sinusoidal heaving motion (t/T = 2/10), and low pressure induced by LEV on the upper foil surface diminished faster than previous cases. This mechanism is bas synchronization between the movement of the foil and the evolution of the vorticity field. For such reasons, this

interaction contributes to form a negative product $C_L \cdot dh/dt$ in this interval. Moreover, the LEV becomes weaker with *D*, and it seems that the mechanism of LEV discussed above does not have essential impact on the pressure distributions. As we can see Figure 6.10 and 6.11, the magnitude of pressure distribution of H1 is smaller than sinusoidal heaving motion. In these non-sinusoidal heaving motion cases, Staying LEV on the foil surface and synchronization between the foil movements and the evolution of vorticity field is crucial points to energy harvesting.

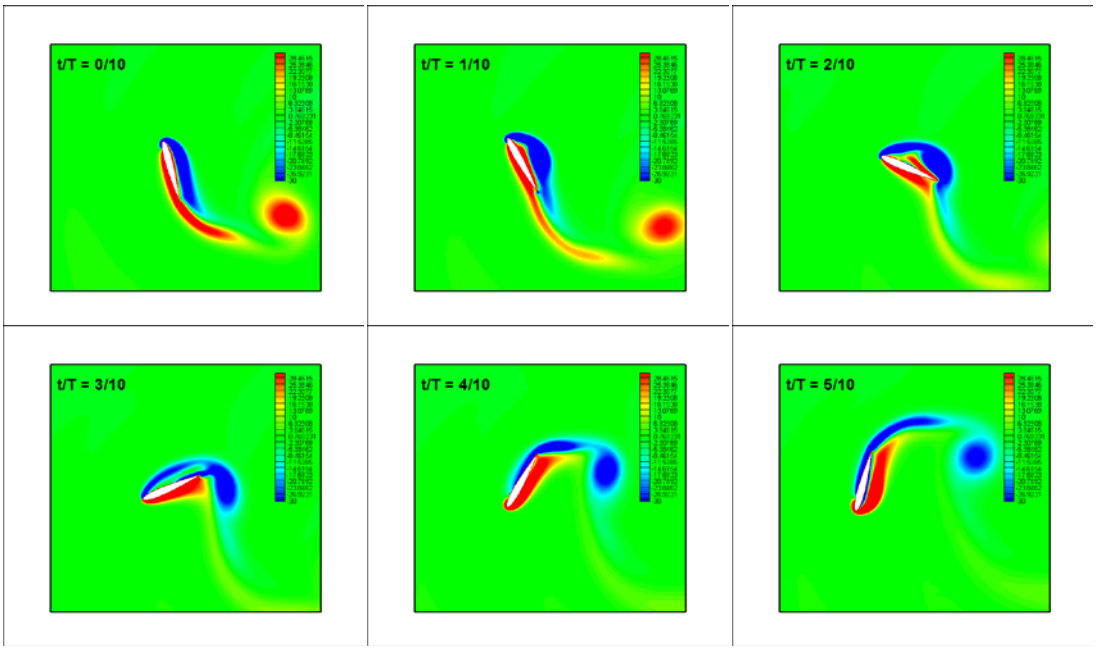

Figure 6.5: Vorticity fields at *f** of 0.15 in sinusoidal heaving motion

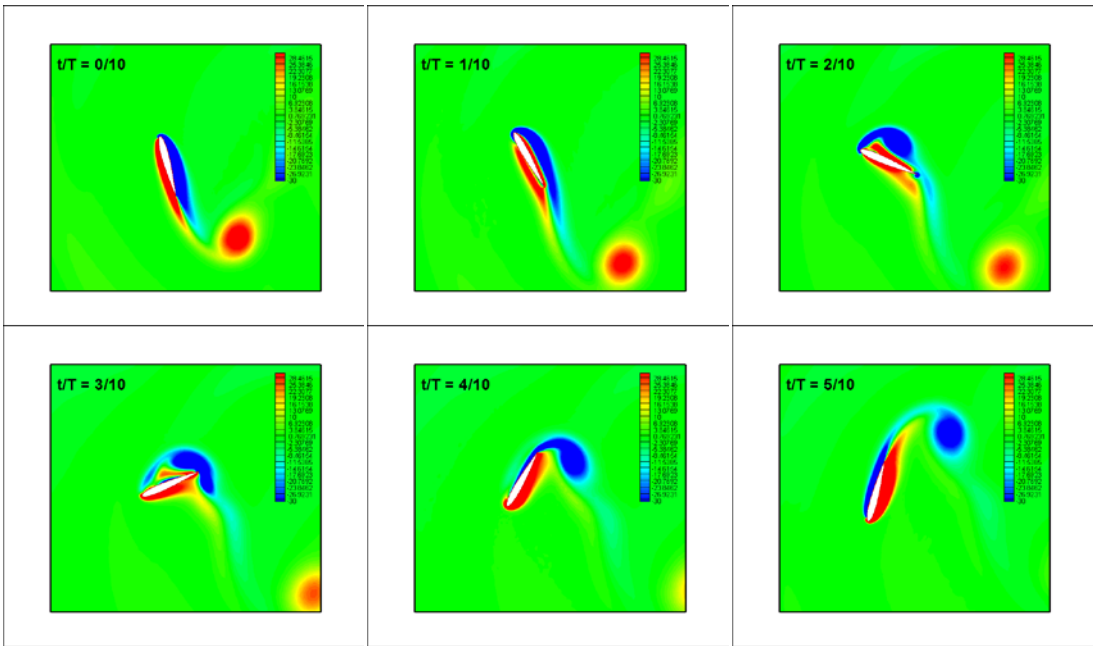

Figure 6.6: Vorticity fields at *f** of 0.15 in H1 (trapezoidal heaving motion)

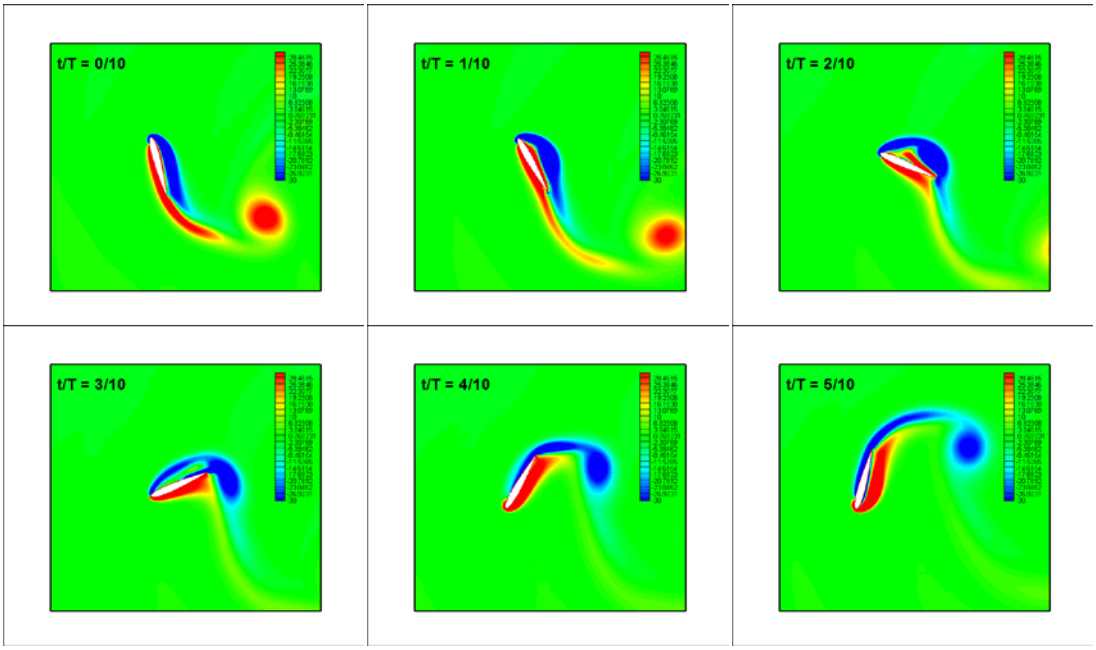

Figure 6.7: Vorticity fields at *f** of 0.15 in H3 (trapezoidal heaving motion)

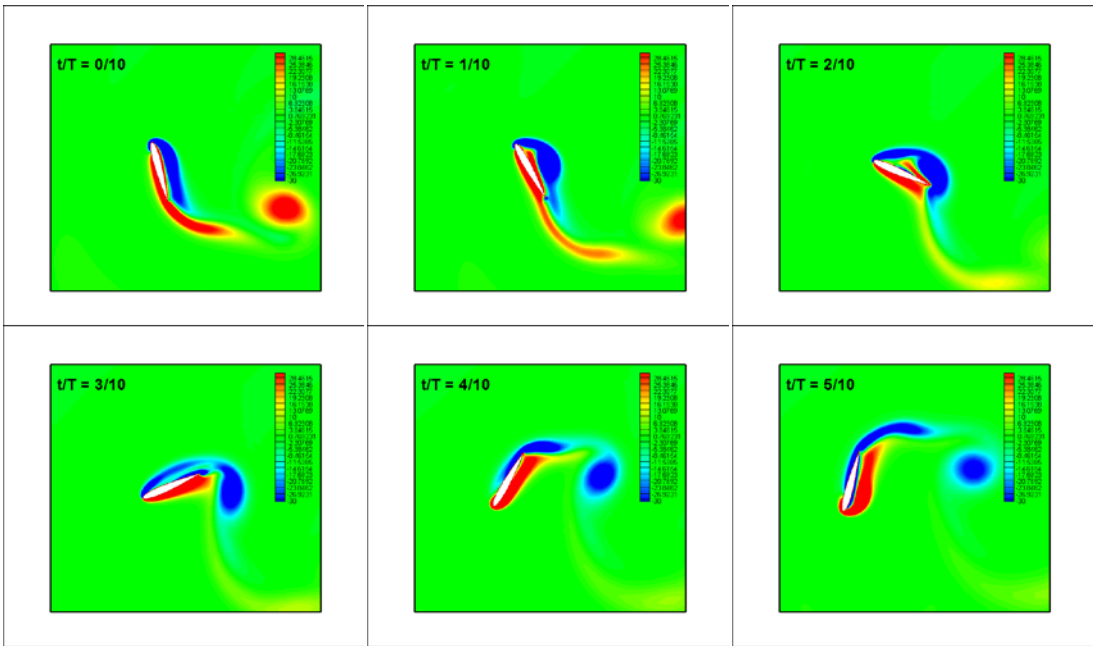

Figure 6.8: Vorticity fields at *f** of 0.15 in H4 (triangular heaving motion)

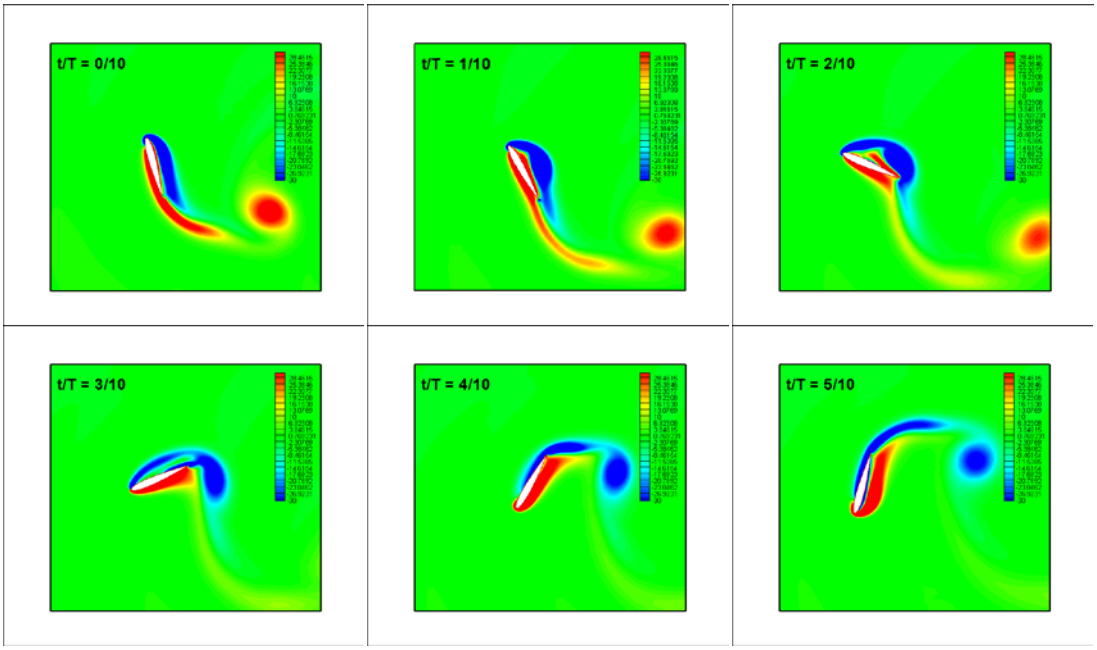

Figure 6.9: Vorticity fields at *f** of 0.15 in H6 (triangular heaving motion)

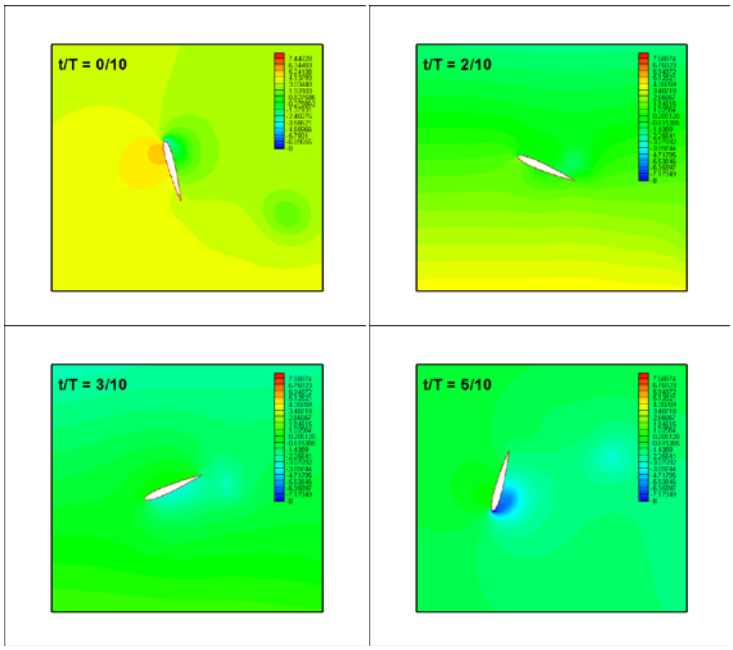

Figure 6.10: Pressure fields at *f** of 0.15 in sinusoidal heaving motion

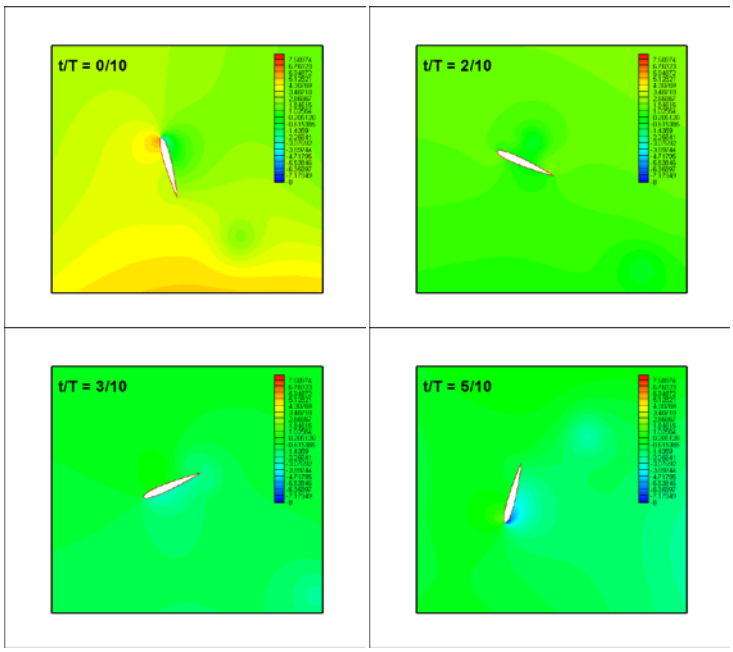

Figure 6.11: Pressure fields at *f** of 0.15 in H1 (trapezoidal heaving motion)

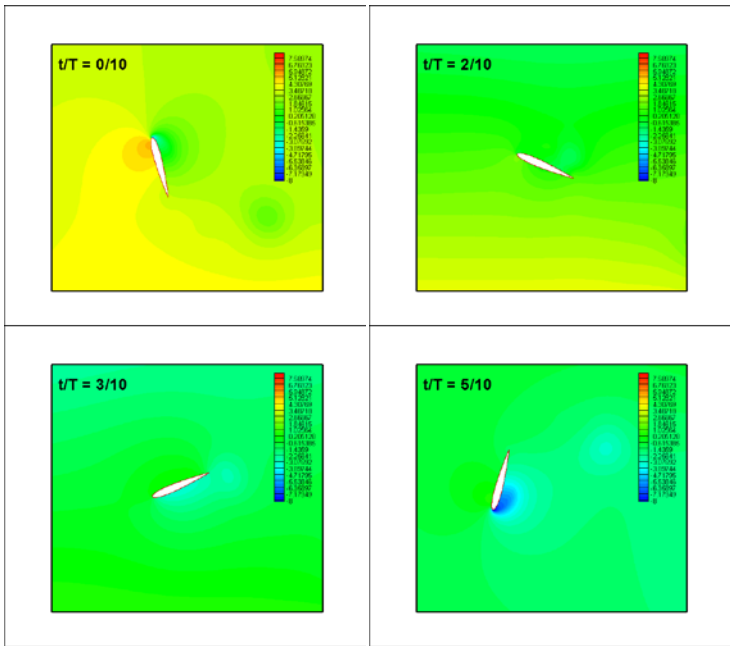

Figure 6.12: Pressure fields at *f** of 0.15 in H3 (trapezoidal heaving motion)

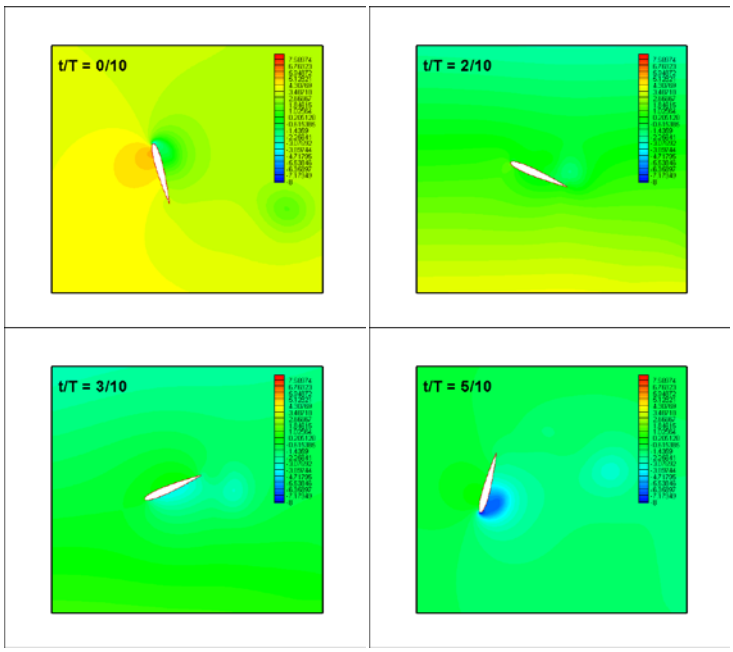

Figure 6.13: Pressure fields at *f** of 0.15 in H4 (triangular heaving motion)

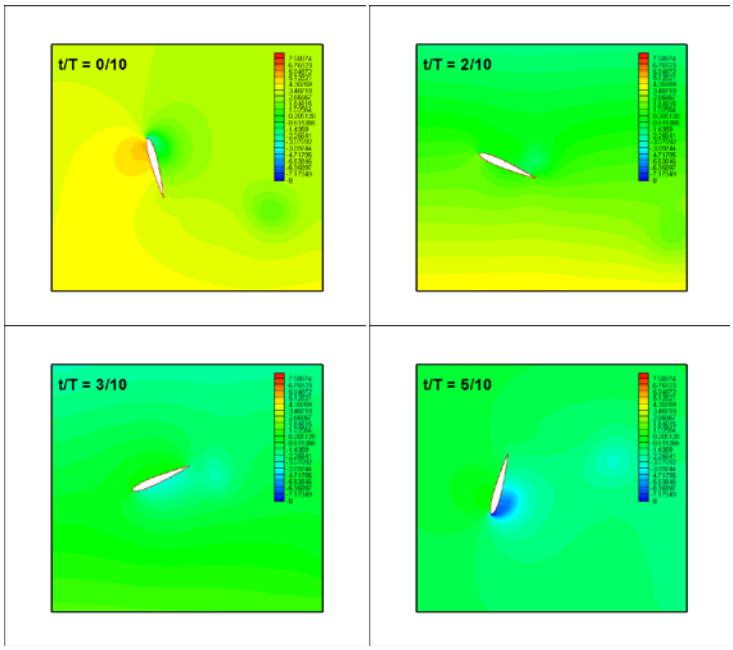

Figure 6.14: Pressure fields at *f** of 0.15 in H6 (triangular heaving motion)

Chapter 7

CONCLUSIONS

This numerical study investigates the potential of the flapping foil for energy harvesting to improve the output power and efficiency with linear shear inlet profiles and non-sinusoidal heaving motions combined with the sinusoidal pitching motion. The investigation covers a wide range of non-dimensional frequencies. In linear shear inlet profile, case of K= 0.2 show the best energy harvesting performance with lower non-dimensional frequencies and its efficiency is better than uniform inlet profile case. This case shows good synchronization between the foil movements and the evolution of vorticity field, so it can useful for getting higher energy harvesting capacity. Trapezoidal heaving motions have zero heaving velocity intervals. These intervals make no contribution to energy harvesting. The vorticity structure and the pressure distribution of triangular heaving motions have similar to that of sinusoidal heaving motion. K= 0.2 in linear shear inlet flow and triangular heaving motion show better performance than uniform flow and sinusoidal heaving motion, respectively. These efficiencies, however, is slightly higher than reference case. Staying LEV on the foil surface and synchronization between the foil movements and the evolution of vorticity field is essential impact to all of cases for power generation.

Further work will focus on the analysis of a 3 dimensional case and the combination of non-sinusoidal pitching and heaving motion for enhancing lift force. We

believe that above conclusions are important for the understanding of physical mechanism and optimal control on energy harvesting devices and thus can suggest guideline to the engineering design of similar devices.

References

[1] W.Shyy *et al.*: “Recent progress in flapping wing aerodynamics and aeroelasticity”. Progress in Aerospace Sciences, 46, 2010, pp. 284-327.

[2] J.M. Anderson, K. Streitlien, D.S. Barret, M.S. Triantafyllou: “Oscillating foils for high propulsive efficiency” J. Fluid Mech. 360, 1998. pp. 41–72.

[3] M.S. Triantafyllou, A.H. Techet, F.S. Hover: “Review of experimental work in biomimetic foils”. IEEE J. Ocean Eng., 29 (3), 2004, pp.585–594.

[4] Z.J. Wang: “Vortex shedding and frequency selection in flapping flight”. J. Fluid Mech., 410, 2000, pp.323–341.

[5] H. Liu, K. Kawachi: “A numerical study of insect flight”. J. Comput. Phys., 146 ,1998 pp.124–156.

[6] R. Rammamutri, W.C. Sandberg: “A three-dimensional computational study of the aerodynamic mechanisms of insect flight”. J. Exp. Biol., 205, 2002, pp1507–1518.

[7] Q. Zhu, M. Wolfgang, D. K. P. Yue, and M. S. Triantafyllou: “Threedimensional flow structures and vorticity control in fish-like swimming”. J. Fluid Mech., 468, 1, 2002.

[8] J. C. Liao, D. N. Beal, G. V. Lauder, and M. S. Triantafyllou: “Fish exploiting vortices decrease muscle activity”. Science 302, 2003, 1566 .

[9] Zhu, Qiang: “Optimal frequency for flow energy harvesting of a flapping foil”. J. Fluid Mech. 675, 2011, pp. 495-517

[10] FLUENT, Software Package, Ver. 6.3, ANSYS, Inc., Lebanon, NH

[11] FLUENT, Software Package, Ver. 12.1, ANSYS, Inc., Lebanon, NH

[12] McKinney, W., and DeLaurier, J.: “The wingmill: An oscillating-wing windmill”. Journal of Energy, 5(2), 1981, pp. 109–115.

[13] Jones KD, Platzer MF.: “Numerical computation of flapping-wing propulsion and power extraction”, AIAA Paper, 1997, No. 97-0826.

[14] Kinsey, T. & Dumas, G.: “Parametric study of an oscillating foil in a power-extraction regime”. AIAA Journal, 46(6), 2008, pp. 1318-1330

[15] Zhu, Q., Haase, M. & Wu, C. H.: “Modeling the capacity of a novel flow-energy

harvester". Appl. Math. Model. 33, 2009, pp. 2207–2218.

[16] Zhu, Q. & Peng, Z.: "Mode coupling and flow energy harvesting by a flapping foil". Phys. Fluids, 21, 2009, 033601

[17] Peng, Z. & Zhu, Q.: "Energy harvesting through flow-induced oscillations of a foil". Phys. Fluids, 21, 2009, 123602

[18] M. F. Platzer, J. Young, and J.C.S. Lai: "Flapping-wing technology: the potential for air vehicle propulsion and airborne power generation", 26th International Congress of the Aeronautical Sciences

[19] M. F. Platzer, M.A. Ashraf, J. Young, and J.C.S. Lai: "Extracting power in jet streams: pushing the performance of flapping wing technology", 27th International Congress of the Aeronautical Sciences

[20] Qing Xiao & Wei Liao: "Numerical investigation of angle of attack profile on propulsion performance of an oscillating foil", Computers & Fluids, 39, 2010, pp.1366-1380

[21] Qing Xiao, Wei Liao, Shuchi Yang, and Yan Peng: "How motion trajectory affects energy extraction performance of biomimic energy generator with an oscillating foil?", Renewable Energy, 37, 2011, pp. 61-75

[22] A. westwood: "Ocean power wave and tidal energy review", Refocis 5, 50, 2004

[23] BioPower systems webpage: http://www.biopowersystems.com/

[24] Hover FS, Haugsdal O, Triantafyllou MS.: "Effect of angle of attack profiles in flapping foil propulsion", J Fluids Struct, 19, 2004, 37e47.

[25] Gordon J. Berman and Z. Jane Wang: "Energy-minimizing kinematisc in hovering insect flight", J. Fluid Mech. vol. 582, 2007, pp. 153-168

[26] Michael H. Dickinson, Fritz-Olaf Lehmann, Sanjay P. Sane: "Wing rotation and the aerodynamic basis of insect flight", Science, vol .284, 1999, no. 5422, pp. 1954-1960

[27] A. Betz, Introduction to the Theory of Flow Machines _Pergamon, Oxford, 1966.

[28] L. Guglielmini & P. Blondeaux: "Propulsive efficiency of oscillating foils," Euro. J. Mech. B/Fluids 23, 255, 2004.